NOW-23: The 2023 National Offshore Wind Data Set

Final Report

Prepared for:

National Offshore Wind Research and Development Consortium

Albany, New York

Julian Fraize
Program Manager

Prepared by:

National Renewable Energy Laboratory

Nicola Bodini

Stephanie Redfern

Alex Rybchuk

Vincent Pronk

Simon Castagneri

Avi Purkayastha

Caroline Draxl

Ethan Young

Billy Roberts

Evan Rosenlieb

Walter Musial

Pacific Northwest National Laboratory

Sheng-Lun Tai

Larry Berg

University of Colorado Boulder

David Rosencrans

Julie K. Lundquist

Veer Renewables

Mike Optis

NOWRDC Contract #147502

December 2023

Notice

This report was prepared by the National Renewable Energy Laboratory and its project partners Pacific Northwest National Laboratory, University of Colorado Boulder, and Veer Renewables in the course of performing work contracted for and sponsored by the National Offshore Wind Research and Consortium (NOWRDC), New York State Energy Research and Development Authority (NYSERDA), and the U.S. Department of Energy (hereafter the "Sponsors"). The opinions expressed in this report do not necessarily reflect those of the Sponsors or the State of New York, and reference to any specific product, service, process, or method does not constitute an implied or expressed recommendation or endorsement of it. Further, the Sponsors, the State of New York, and the contractor make no warranties or representations, expressed or implied, as to the fitness for particular purpose or merchantability of any product, apparatus, or service, or the usefulness, completeness, or accuracy of any processes, methods, or other information contained, described, disclosed, or referred to in this report. The Sponsors, the State of New York, and the contractor make no representation that the use of any product, apparatus, process, method, or other information will not infringe privately owned rights and will assume no liability for any loss, injury, or damage resulting from, or occurring in connection with, the use of information contained, described, disclosed, or referred to in this report.

NYSERDA makes every effort to provide accurate information about copyright owners and related matters in the reports we publish. Contractors are responsible for determining and satisfying copyright or other use restrictions regarding the content of reports that they write, in compliance with NYSERDA's policies and federal law. If you are the copyright owner and believe a NYSERDA report has not properly attributed your work to you or has used it without permission, please email print@nyserda.ny.gov.

Information contained in this document, such as web page addresses, are current at the time of publication.

Acknowledgments

The authors would like to thank the members of the project advisory board for their continuous feedback and support throughout the project. We would like to extend a special thanks to Shell for agreeing to share lidar data in the Gulf of Mexico. We also thank Billy Roberts and Evan Rosenlieb for producing the wind resource maps included in this report.

This research was performed using computational resources sponsored by the U.S. Department of Energy's Office of Energy Efficiency and Renewable Energy and located at the National Renewable Energy Laboratory.

This work was authored in part by the National Renewable Energy Laboratory, operated by Alliance for Sustainable Energy, LLC, for the U.S. Department of Energy (DOE) under contract no. DE-AC36-08GO28308. Funding was provided by the U.S. Department of Energy Office of Energy Efficiency and Renewable Energy Wind Energy Technologies Office. The views expressed in the article do not necessarily represent the views of the DOE or the U.S. Government. The U.S. Government retains and the publisher, by accepting the article for publication, acknowledges that the U.S. Government retains a nonexclusive, paid-up, irrevocable, worldwide license to publish or reproduce the published form of this work, or allow others to do so, for U.S. Government purposes.

Table of Contents

List of Figures

List of Tables

Acronyms and Abbreviations

ASIT	air-sea interaction tower
asl	above (mean) sea level
CA20	(first-generation) 20-year wind resource data set for offshore California
cRMSE	centered (or unbiased) root-mean-square error
DOE	U.S. Department of Energy
EEZ	Exclusive Economic Zone
GOES-16	Geostationary Operational Environmental Satellite 16
HRRR	High-Resolution Rapid Refresh
IMU	inertial measurement unit
IQR	inter-quartile range
LSM	land surface model
MUR25	Multi-scale Ultra-high Resolution
MVCO	Martha's Vineyard Coastal Observatory
MYNN	Mellor-Yamada-Nakanishi-Niino
NASA	National Aeronautics and Space Administration
NCAR	National Center for Atmospheric Research
NCEP	National Center for Environmental Prediction
NDBC	National Data Buoy Center
NOW-23	2023 National Offshore Wind (data set)
NREL	National Renewable Energy Laboratory
NWP	numerical weather prediction (model)
NYSERDA	New York State Energy Research and Development Authority
OCS	Outer Continental Shelf
OSTIA	Operational Sea Surface Temperature and Sea Ice Analysis
PBL	planetary boundary layer
PDF	probability density function
PNNL	Pacific Northwest National Laboratory
rex	Resource eXtraction (tool)
RTG	real-time global
SST	sea surface temperature
TI	turbulence intensity
TLP	tension-leg platform
TKE	turbulence kinetic energy
WIND	Wind Integration National Dataset
WRF	Weather Research and Forecasting
YSU	Yonsei University

Executive Summary

In this report, we present the latest wind resource data specifically tailored for offshore regions in the United States. The data set, known as the 2023 National Offshore Wind data set (NOW-23), has been developed by the National Renewable Energy Laboratory (NREL) and its partners and surpasses the offshore component of the previous resource data set, the Wind Integration National Dataset (WIND) Toolkit, which was released approximately 10 years ago. The WIND Toolkit has been widely utilized by stakeholders involved in wind resource assessments across the continental United States. However, with significant advancements in numerical weather prediction modeling over the past decade, the NOW-23 data set incorporates the latest research and development progress to provide stakeholders with an updated and cutting-edge resource for offshore wind analysis.

The NOW-23 data set is created using the Weather Research and Forecasting (WRF) model, and its output is available, as for its predecessor, at 5-minute time resolution and 2-kilometer horizontal spatial resolution. However, the NOW-23 data set improves upon the WIND Toolkit through:

1. A modeling period of at least 20 years (and as long as 23 years in selected regions), starting in 2000 (compared to the 7-year 2007–2013 modeling period in the WIND Toolkit).

2. For several offshore regions, a region-specific sensitivity analysis, driven by an ensemble of WRF simulations, to assess the most adequate region-specific WRF setup.

3. An updated WRF model, from Version 3.4 used in the WIND Toolkit to Version 4.2.1 used for the NOW-23 data set, which incorporates significant research advancements.

4. The use of the state-of-the-art reanalysis product ERA5 (which supersedes the older ERA-Interim used in the WIND Toolkit) to provide atmospheric forcing at the WRF domain boundaries.

Figure 1 shows the NOW-23 mean wind speed at 160 meters (m) above sea level (asl), which we use as proxy for hub height of a commercial offshore wind turbine in this report across all regions.

Figure 1. Map of the long-term mean wind speed at 160 m asl across the United States offshore regions, as modeled in the NOW-23 data set. Taken from Bodini et al. (in review).

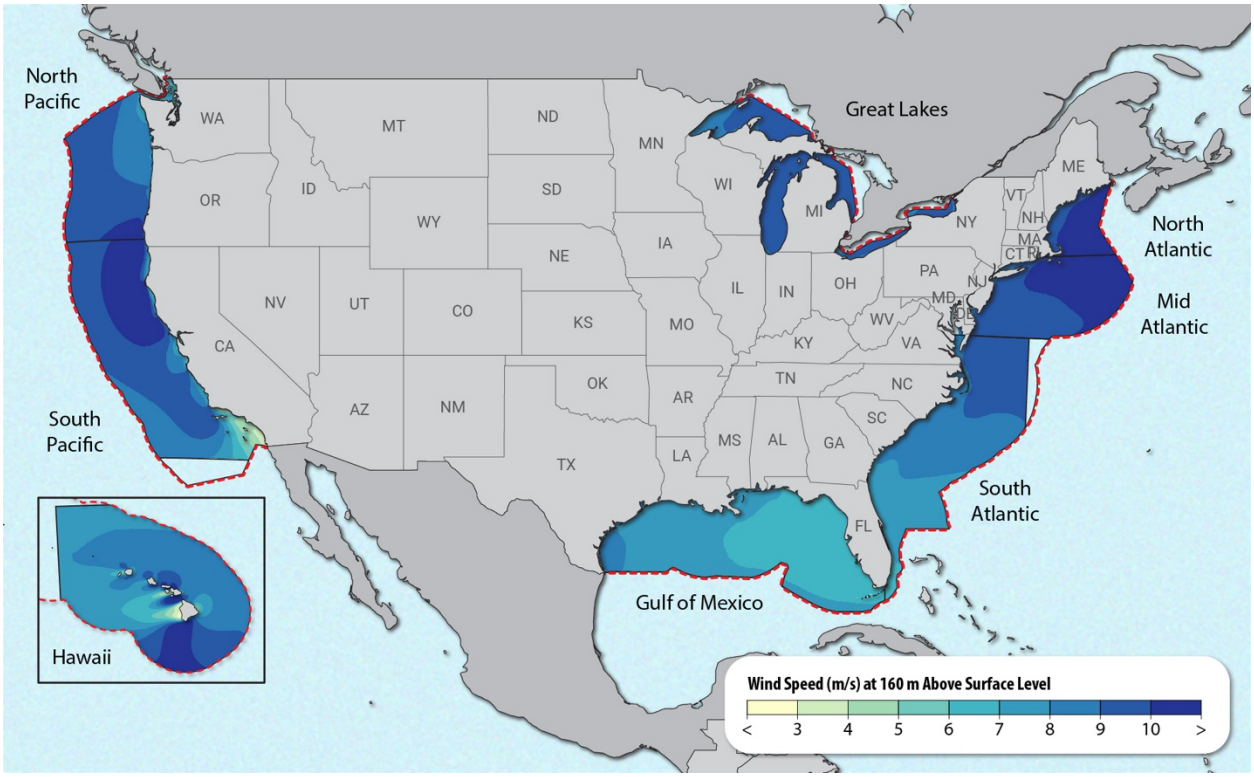

In this report, we summarize the region-specific approach adopted to develop the NOW-23 data set. We also provide details on the uncertainty quantification efforts connected to the NOW-23 data set, and we provide users with information on how to easily access and handle the NOW-23 data. Finally, we summarize parallel research efforts to assess wake impacts in the Mid-Atlantic region (NOW-WAKES data set) and to incorporate turbulence intensity capabilities into WRF.

1 Introduction

This report presents the work conducted by the National Renewable Energy Laboratory (NREL) and its partners Pacific Northwest National Laboratory (PNNL), University of Colorado Boulder, and Veer Renewables to develop a cutting-edge offshore wind resource data set for all regions (except for Alaska) in the United States. This data set, named NOW-23 (2023 National Offshore Wind data set), represents a significant advancement in wind resource data.

In 2013, NREL introduced the Wind Integration National Dataset (WIND) Toolkit (Draxl et al. 2015a; Draxl and Hodge 2015b), a comprehensive wind resource data set covering the entire continental United States from 2007 to 2013. This data set utilized the Weather Research and Forecasting (WRF) model (Skamarock et al. 2019) and became widely used in wind energy assessment. However, since then, significant progress has been made in the field of numerical weather prediction (NWP) models, also based on results from major field campaigns (e.g., Wilczak et al. 2015; Shaw et al. 2019; Fernando et al. 2019) and the availability of new reanalysis products (e.g., Hersbach et al. 2020). Additionally, it has been recognized that longer-term data sets, spanning at least 20 years, are essential for a robust wind resource evaluation.

To ensure that stakeholders have access to the most accurate and up-to-date wind resource data, NREL and its partners have undertaken the task of developing a next-generation product to replace the WIND Toolkit, specifically tailored for offshore wind energy analysis. The NOW-23 data set provides a validated offshore wind resource atlas for all U.S. offshore waters, covering a minimum of 20 years. It offers data at a 5-minute time resolution, 2-kilometer (km) horizontal resolution, and up to 500 meters (m) above the surface. This report summarizes the NOW-23 data set, outlines efforts to quantify the uncertainty associated with the data set, presents a 1-year post-construction data set to assess wind turbine and wind plant wakes in the Mid-Atlantic region, and describes efforts to implement turbulence intensity capabilities into WRF. A separate report will document the parallel effort to create the next generation of the onshore component of the WIND Toolkit.

2 The NOW-23 data set

In this section, we summarize the development and main characteristics of the NOW-23 data set for all the regions completed as part of this work. A more detailed description is included in Bodini et al. (in review).

2.1 Numerical setup

To develop the NOW-23 data set, we adopt a regional approach, where separate numerical simulations are conducted for each offshore region. The setup for these simulations is chosen (in most regions) based on validation against available observations, allowing for customization to capture region-specific wind resource phenomena. The eight regional domains of the NOW-23 data set are depicted in Figure 2. We note that WRF domains are rectangular-shaped. However, to minimize storage requirements for the NOW-23 data files, most regional data sets are masked after the WRF simulations are completed. This masking is based on the Exclusive Economic Zone (EEZ), which extends approximately 212 nautical miles from the coast and represents the jurisdictional area over natural resources, including wind.

Figure 2. Map of the regional WRF domains used to build the NOW-23 data sets, masked at the limit of the Exclusive Economic Zone of the countries with jurisdiction on the offshore regions being considered. Taken from Bodini et al. (in review).

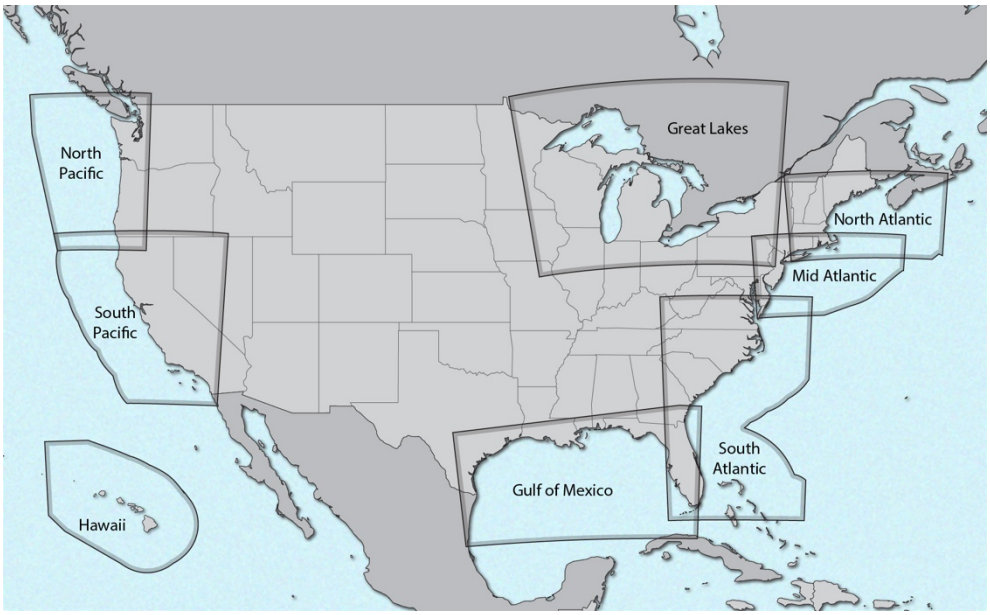

Table 1 provides an overview of the common attributes for all the WRF simulations utilized to construct NOW-23. The simulations are executed in 1-month segments, which are then concatenated at each grid

cell during the post-processing phase. A spin-up period of 2 days is included to allow the model to stabilize from the initial conditions imposed on WRF. This means that, for instance, the May 2015 simulation actually begins on April 29, 2015. The use of 1-month segments is driven by the need to minimize the number of restart periods, as each restart can introduce false ramps in grid applications. Additionally, this approach helps reduce the overall simulation time, leveraging the parallel computing capabilities provided by NREL's supercomputer. It is important to note that we have not observed any degraded performance in modeled wind speed over time within each calendar month.

Table 1. WRF common attributes used in all the simulations used to build the NOW-23 data set.

Feature	Specification
WRF version	4.2.1
Nesting	6 km, 2 km
Vertical levels	61
Near-surface-level heights (meters)	12, 34, 52, 69, 86, 107, 134, 165, 200
Atmospheric nudging	Spectral nudging on 6-km domain, applied every 6 hours
Microphysics	Ferrier
Longwave radiation	Rapid Radiative Transfer Model
Shortwave radiation	Rapid Radiative Transfer Model
Topographic database	Global Multi-Resolution Terrain Elevation Data from the United States Geological Service and National Geospatial-Intelligence Agency
Land-use data	Moderate Resolution Imaging Spectroradiometer 30s
Cumulus parameterization	Kain-Fritsch

Table 1 does not list some crucial attributes that need to be configured before running the WRF simulations. For the majority of the regions considered in this work, prior to conducting the long-term simulation for a region, we consider and run multiple WRF setups (i.e., a WRF ensemble) over a 1-year period. These setups are then validated against available observations to determine the most suitable configuration for long-term offshore wind resource assessment in each region.

To determine which WRF setups to include in the validation experiments, we leverage recent research on the sensitivity of WRF-modeled wind speeds to the setup choices. Optis et al. (2020a) provide a detailed list of studies examining the impact of WRF setup choices on wind speed predictions. Notably, the New European Wind Atlas developed by Hahmann et al. (2020) and NREL's offshore analysis in collaboration with Rutgers Center for Ocean Observing Leadership (Optis et al. 2020b) are highlighted as comprehensive efforts in this field. Based on recent literature, five setup choices are identified as the most influential on the WRF-modeled wind resource: reanalysis forcing product, planetary boundary layer

(PBL) scheme, sea surface temperature (SST) product, land surface model (LSM), and surface layer scheme. For each region where a short-term WRF ensemble is conducted, a subset of setups is chosen by combining various options for the aforementioned setup choices:

- **Reanalysis forcing product**: We consider the ERA5 reanalysis product developed by the European Centre for Medium-Range Weather Forecasts (Hersbach et al. 2020) and the Modern-Era Retrospective analysis for Research and Applications, Version 2 (Gelaro et al. 2017), developed by the National Aeronautics and Space Administration (NASA).
- **Planetary boundary layer scheme**: We consider the Mellor-Yamada-Nakanishi-Niino (MYNN, Nakanishi and Niino, 2009) and the Yonsei University (YSU) (Hong et al. 2006) PBL schemes.
- **Sea surface temperature product**: We consider the Operational Sea Surface Temperature and Sea Ice Analysis (OSTIA) data set produced by the United Kingdom Met Office (Donlon et al. 2012; Hirahara et al. 2016) and the National Center for Environmental Prediction (NCEP) Real-Time Global (RTG) SST product (National Weather Service 2014).
- **Land surface model**: We consider the Noah LSM and the updated Noah-Multiparameterization LSM (Niu et al. 2011).
- **Surface layer scheme:** We consider the MM5 (Grell et al. 1994; Jiménez et al. 2012) and MYNN (Olson et al. 2021) surface layer schemes.

2.2 Observational data sets used for model validation

In NOW-23, we utilize offshore or coastal observations in the majority of the modeled offshore regions to determine the best WRF configuration. Figure 3 displays all the observational data sets used in the development of NOW-23. Typically, we incorporate data from available offshore lidars, alongside observations from near-surface buoys obtained from the National Data Buoy Center (NDBC) and coastal radars, as resources allow. A comprehensive description of the observational data sets can be found in the overview journal article mentioned at the beginning of this section (Bodini et al. in review). In the North Pacific and Hawaii regions, there is a lack of publicly accessible hub-height offshore wind speed observations. As a result, the WRF setup for these regions is based on the findings from the initial stages of the project in the South Pacific and the Mid-Atlantic domains. Future work for these two regions is outlined in Section 2.6.

Figure 3. Map of the observational data sets used to validate the NOW-23 data set. Taken from Bodini et al. (in review).

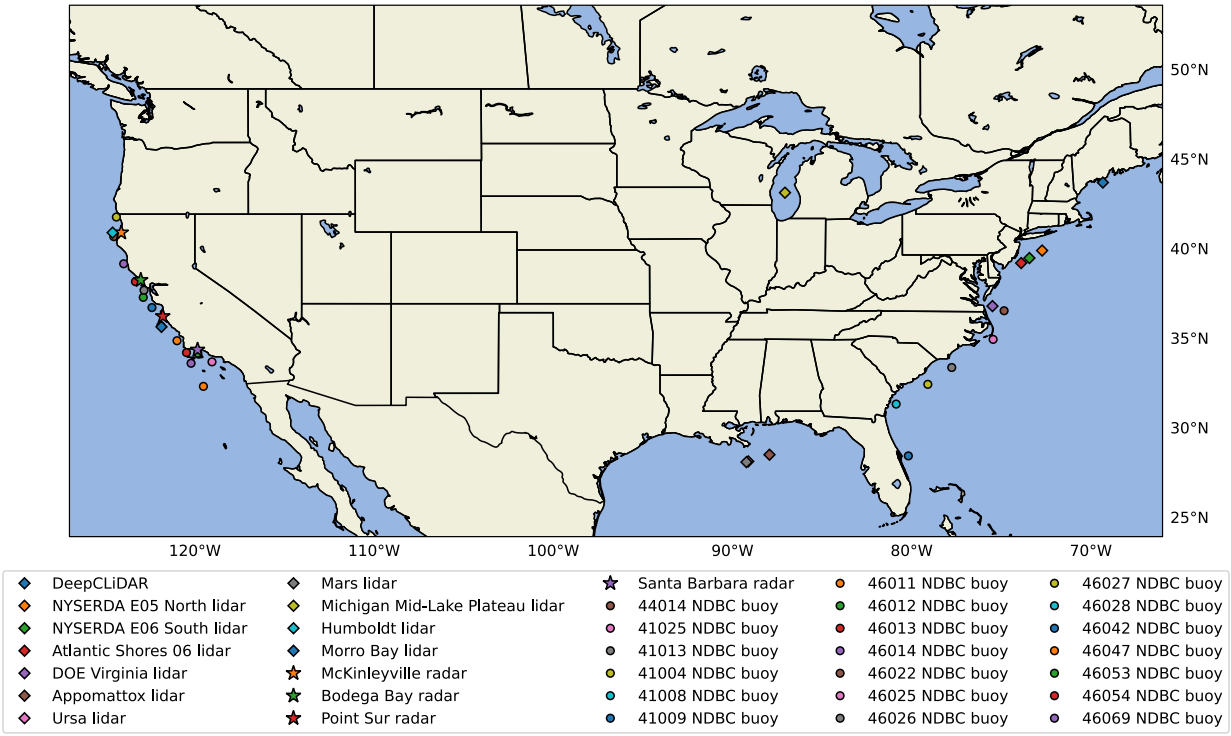

Our validation methodology follows the recommended guidelines outlined in Optis et al. (2020). We employ multiple error metrics to compare the modeled and observed wind speed and select the appropriate model setup. These metrics include bias, centered (or unbiased) root-mean-square error (cRMSE), Pearson's correlation coefficient (r), and a comparison of the standard deviation between modeled and observed wind speed. An ideal model setup would exhibit zero bias, zero cRMSE, a correlation coefficient of 1, and a modeled wind speed standard deviation equal to that of the observed wind speed. To succinctly summarize these three metrics, we adopt the Taylor diagram (Taylor 2001), which is a mathematical plot that visually represents the model's performance in terms of cRMSE, r, and standard deviation.

2.3 Choice of the long-term WRF setup

The region-specific results of the validation are described in detail in the Bodini et al. (in review) overview paper. As a result of the validation, two WRF setups were used for the different regions, as outlined in Table 2 and Table 3.

Table 2. Selected WRF setup for the long-term NOW-23 simulation in the North Atlantic, Mid-Atlantic, Great Lakes, North Pacific, and Hawaii regions.

WRF ensemble member name	Reanalysis product	PBL scheme	SST product	LSM	Surface layer scheme
WRF1	ERA5	MYNN	OSTIA	NOAH	MYNN

Table 3. Selected WRF setup for the long-term NOW-23 simulation in the South Atlantic, Gulf of Mexico, and South Pacific regions.

WRF ensemble member name	Reanalysis product	PBL scheme	SST product	LSM	Surface layer scheme
WRF4	ERA5	YSU	OSTIA	NOAH	MM5

The NOW-23 data set starts on Jan. 1, 2000, for all offshore regions. For North Pacific and Hawaii, NOW-23 goes until Dec. 31, 2019. For North Atlantic, Mid-Atlantic, South Atlantic, Gulf of Mexico, and Great Lakes, NOW-23 goes until Dec. 31, 2020. For the South Pacific region, the data set goes until Dec. 31, 2022.

2.4 Modeled wind resource in the South Pacific region: from CA20 to NOW-23

The initial focus of the development of this long-term wind resource data set was on the South Pacific region (i.e., offshore California). This was part of a pilot project funded by the Bureau of Ocean Energy Management, and the data set has undergone revisions throughout its development.

The creation of the first version of the 20-year data set for the California Outer Continental Shelf (OCS), known as "CA20," is described in Optis et al. (2020a).

The selection of the WRF setup for the CA20 data set was based on validation against available observations at the time, including data from near-surface NDBC buoys and coastal radars. The validation results obtained in the Mid-Atlantic region also played a role in the selection process. The CA20 data set covers the period from Jan. 1, 2000, to Dec. 31, 2019, and was generated using the ERA-5 reanalysis product, the MYNN PBL scheme, the OSTIA SST product, the NOAH LSM, and the MYNN surface layer scheme.

However, the measurements available for validating the CA20 model were not ideal. The buoys provided measurements close to the surface, which were insufficient for determining the wind resource at the relevant heights for wind energy purposes. Although coastal radars provided measurements at the relevant heights, validating the WRF model at their locations became uncertain due to significant meteorological gradients at the land-ocean interface. Furthermore, the results from the Mid-Atlantic validation could not be directly applied to the U.S. West Coast due to distinct domain-specific processes and features that might require a different optimal WRF setup. It was also acknowledged that the absence of floating lidar observations in the California OCS posed a significant limitation to the analysis and initial validation of the CA20 data set.

To address this limitation, two floating lidars were deployed in the region in late 2020: one near the Humboldt wind energy lease area and one near the Morro Bay wind energy lease area. The original WRF setup used in the CA20 data set was rerun over the period from October 2020 to September 2021 and compared with the observations collected by the two lidars. This comparison revealed a notable bias in the CA20 modeled data. The impact of this bias on energy assessments in the California OCS is discussed in Bodini et al. (2022).

Further analysis indicated that the choice of the planetary boundary layer scheme was primarily responsible for the bias in the CA20 data set. The MYNN PBL scheme, in particular, overestimated atmospheric stability, especially at Humboldt, leading to reduced vertical turbulent mixing. This allowed for the acceleration of hub-height winds, intensified low-level jets, and higher-amplitude inertial oscillations. Additionally, during synoptic-scale northerly flows driven by the North Pacific High and inland thermal low, simulations using the MYNN PBL scheme showed a coastal warm bias in selected case studies. This bias altered the boundary layer thermodynamics through a thermal wind mechanism, contributing to the modeled wind speed bias.

Further investigations revealed that the YSU PBL scheme significantly reduced the bias at both Humboldt and Morro Bay. Due to the strong performance of the YSU-based runs in offshore California, an updated version of the data set using the YSU PBL scheme has been produced and is now part of NOW-23. The results of this in-depth analysis, additional validation against floating lidars and coastal radars, and a description of the updated data set will be presented in an additional NREL technical report that will be published in fall 2023.

2.5 Long-term wind resource in NOW-23

The long-term mean wind resource as modeled in NOW-23 is shown in the map in Figure 4, at 160 m asl. In general, we find a strong mean wind resource across the majority of the modeled regions. On the U.S. East Coast, we observe a north-to-south gradient that reduces the mean wind speed by at least 3 m s^{-1} from Maine to Florida. In the Gulf of Mexico, we see an east-to-west gradient, with the strongest wind speeds recorded in the western side of the Gulf. In the overview paper (Bodini et al. in review), we also present, for each offshore region, an analysis of the diurnal and seasonal variabilities of the hub-height wind speed as well as a comparison with the prior generation data set, the WIND Toolkit.

Figure 4. Map of the long-term mean wind speed at 160 m asl across the U.S. offshore regions, as modeled in the NOW-23 data set. Taken from Bodini et al. (in review).

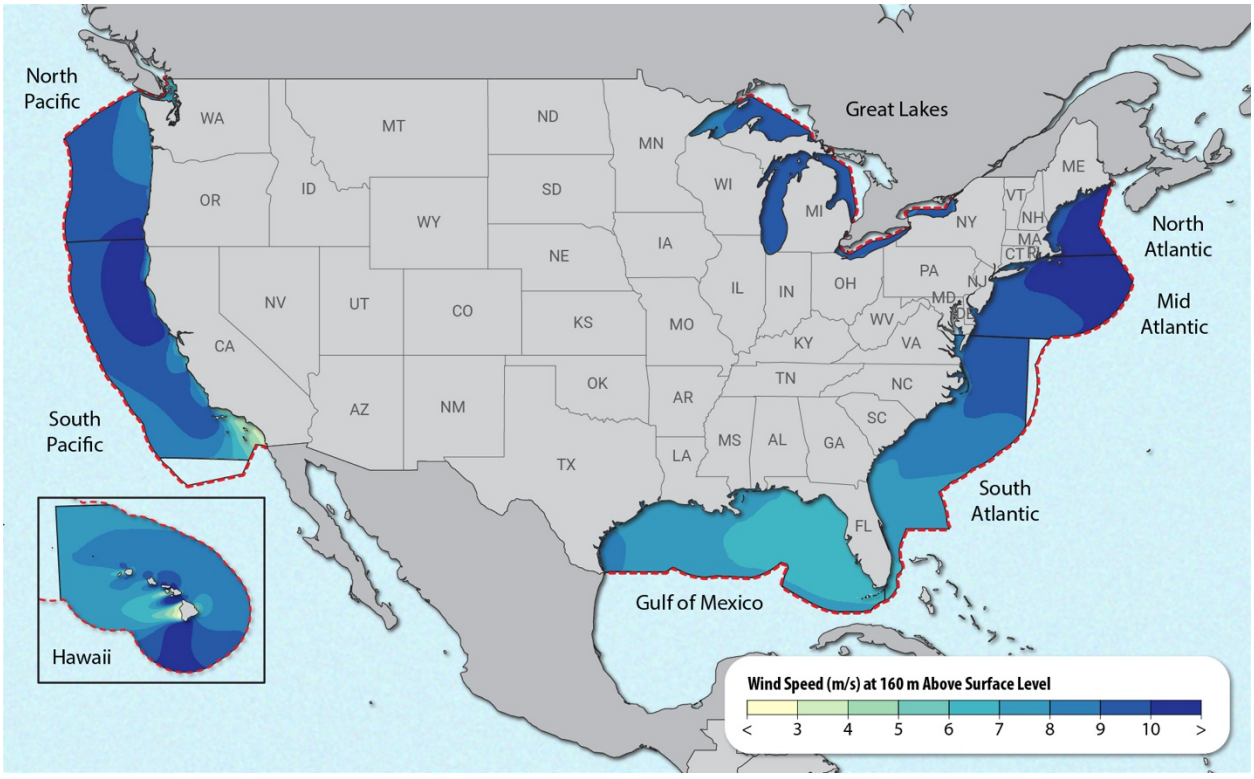

2.6 Future work

As noted above, no validation with observations was performed in the North Pacific and Hawaii regions.

After identifying a significant wind speed bias in the South Pacific data set generated using the MYNN PBL parameterization, we expanded our investigation to the North Pacific coast. This initial assessment involved comparing two WRF simulations with different physics configurations for the year 2020. The

first simulation replicated the setup used for the main 20-year run in this region, and the second simulation utilized the YSU PBL scheme and the MM5 surface layer parameterization. Consistent with the South Pacific data set, we found that the mean wind speeds were stronger off the coast in the MYNN/MYNN setup compared to the YSU/MM5 setup (Figure 5). Specifically, for October 2020, which had previously exhibited a significant positive wind speed bias in the CA20 simulations, the coastal differences exceeded 3 m s^{-1}.

Although there is still a lack of hub-height observations for offshore wind in the region, model validation can be conducted using near-surface buoy data and onshore observations. Leveraging the available observations will be crucial to evaluate the accuracy of the selected WRF setup in the region. However, this aspect will require further work, subject to the availability of funding.

Figure 5. 100-m mean wind speed differences between the MYNN and YSU simulations (MYNN-YSU) in the North Pacific region, averaged for (a) all of 2020 and (b) October 2020.

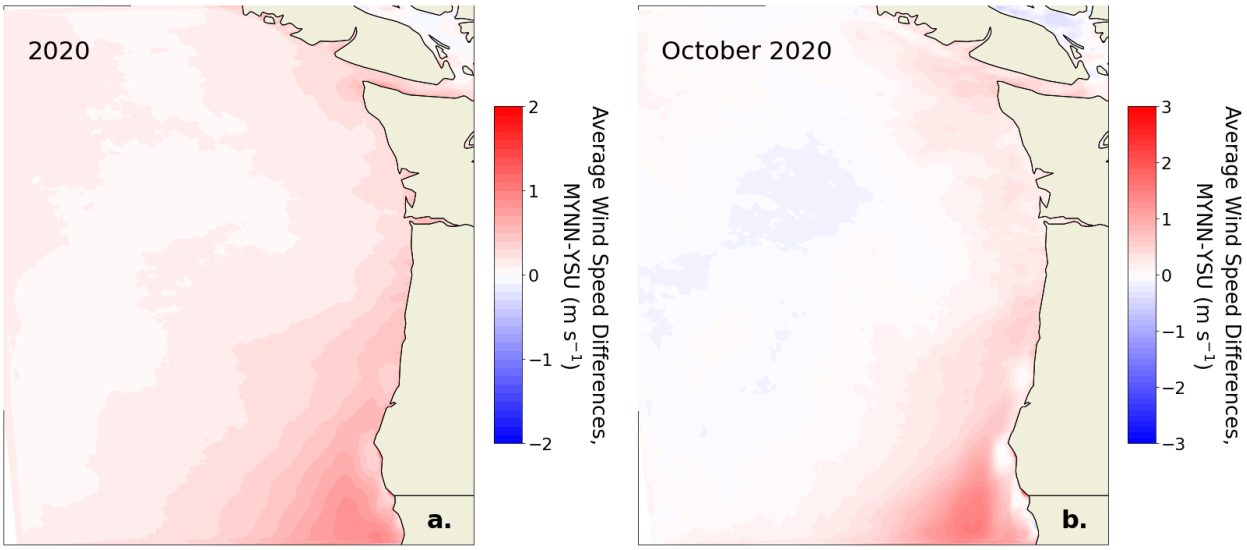

In the case of Hawaii—the other region where no validation against observations was performed to select the WRF setup for the NOW-23 data set—a floating lidar was deployed in December 2022 by PNNL in the region. The observations collected by this instrument will be vital for assessing the accuracy of the chosen WRF setup in the Hawaii region. However, similar to the North Pacific, further work will be contingent upon funding availability.

In the interim, NREL advises stakeholders interested in utilizing the NOW-23 data set in the North Pacific and Hawaii regions to exercise caution due to the aforementioned limitations.

2.7 Data availability

The complete NOW-23 data set is openly accessible through Amazon Web Services at DOI 10.25984/1821404. The data is available in two formats: HDF5 and WRG files.

The HDF5 files are provided for each offshore region and are available at both 5-minute resolution and as hourly averages. These files contain the following variables:

- Planetary boundary layer height (m)
- Pressure at 0 m, 100 m, 200 m, and 300 m (Pa)
- Temperature at 2 m, 10 m, 20-m intervals between 20 m and 300 m, 400 m, and 500 m (°C)
- Wind direction at 10 m, 20-m intervals between 20 m and 300 m, 400 m, and 500 m (° from N)
- Wind speed at 10 m, 20-m intervals between 20 m and 300 m, 400 m, and 500 m ($m\ s^{-1}$)
- Friction velocity at 2 m ($m\ s^{-1}$)
- Sea surface temperature (°C)
- Skin temperature (°C)
- Surface heat flux ($W\ m^{-2}$)
- Relative humidity at 2 m (%)
- Inverse Monin-Obukhov length at 2 m (m^{-1})
- Roughness length (m).

To facilitate data extraction and manipulation from the large NOW-23 files, NREL has developed the REsource eXtraction (rex) tool. Detailed instructions on how to install and use rex can be found at nrel.github.io/rex. Rex allows users to extract a subset of variables for a specific location or a customized region as well as automatically interpolate wind speed data to a desired height. In the near future, NREL will develop a user-friendly interface for visualizing and downloading the NOW-23 data, which will replace the retired NREL Wind Prospector.

The WRG file format, an industry-standard format for modeled wind resource data sets, is also available for the NOW-23 data. WRG files provide wind rose information at specific heights for each modeled grid cell. However, it is important to note that converting the data to the WRG format results in the loss of temporal information and other atmospheric parameters, retaining only wind speed and direction. Despite this limitation, WRG files have been widely used for offshore wind resource assessment. Typically, consultants sell WRG files at a significant cost. By providing NOW-23 WRG files at no charge, NREL eliminates this cost burden for offshore wind stakeholders and offers an additional modeled data set for integrating into energy production estimates and calculating wind uncertainty. For the NOW-23 data sets, NREL has provided WRG files calculated at 160 m above ground level and at 30° wind direction sector

bins. An open-source codebase (www.github.com/NREL/wrg_maker) has also been released, enabling stakeholders to generate additional WRG files from the NOW-23 data set if desired.

For any technical support related to the NOW-23 data set, inquiries can be directed to windtoolkit@nrel.gov.

3 Uncertainty quantification

As part of the project, significant effort was spent to provide stakeholders with uncertainty information. We tackled this aspect from different points of view, which are briefly summarized in the next paragraphs. For each topic listed below, we refer to peer-reviewed articles we published as part of this project to learn more about the details of the work done.

3.1 Sensitivity to sea surface temperature

Given the offshore focus for the NOW-23 data set, one of the first aspects we consider is the sensitivity of the modeled wind speed to the SST product used to force the WRF simulations.

The role of SST in offshore wind resource assessment is an important yet relatively unexplored aspect. Usually, models use reanalysis data sets, which provide daily SST products. However, these daily products may not capture significant variations in SSTs that occur on finer timescales compared to observations. Consequently, model results may not correctly represent shorter-lived events such as sea breezes and low-level jets that are influenced by SSTs. To improve the forecasting of these events, hourly SST products may be more useful.

In this part of the project research, we examine the sensitivity of the WRF model to different SST products in the Mid-Atlantic domain. We consider three different data sets: OSTIA (selected and used for the NOW-23 data set in all considered regions), the Multi-scale Ultra-high Resolution (MUR25) SST analysis, and SSTs from the Geostationary Operational Environmental Satellite 16 (GOES-16).

We find that OSTIA and GOES-16 SSTs validate better against buoy observations than MUR25, so they are selected for further model simulation analysis, and MUR25 is discarded from further consideration. We run model simulations with the two selected SST products for June and July 2020, and find that OSTIA SSTs validate better against in situ observations taken via a buoy array in the region. However, both products result in comparable hub-height wind characterization performance on monthly timescales. During flagged events lasting less than 30 hours that show statistically significant wind speed deviations between the two simulations, both simulations demonstrate similar validation performance, with GOES-16 winds validating nominally better than OSTIA winds.

The results of this analysis are described in detail in Redfern et al. (2023).

3.2 Boundary condition and parametric uncertainty

Next, we focused on more broadly characterizing the uncertainty in the long-term wind resource modeled in the NOW-23 data sets. In fact, while NWP models are a useful tool for characterizing the wind resource offshore, where measuring hub-height wind speed can be challenging, their wind speed representation comes with inherent uncertainty.

Initially, our focus was on understanding the boundary condition and parametric uncertainty in modeled wind speed. The choices made regarding the setup and inputs of NWP models directly influence the predicted wind speeds and the associated uncertainty. To estimate the uncertainty related to the boundary condition and model parameters, running an ensemble of model setups is required. However, generating long-term data over a large area using such ensembles can be computationally demanding. To address this, we proposed two alternative approaches. Firstly, we utilized a short-term mesoscale ensemble, specifically a 1-year ensemble used for selecting the model setup in various offshore regions. Secondly, we conducted a single model run for the desired long-term period, such as the 20+ year NOW-23 run. We quantified the uncertainty of hub-height wind speed boundary condition and parameters by calculating the normalized standard deviation of the short-term model ensemble. Then, we employed a gradient-boosting model and an analog ensemble approach to extend this uncertainty estimation to the entire 20-year period (as depicted in Figure 6).

Figure 6. Qualitative illustration of the concept used to temporally extrapolate the modeled wind speed boundary condition and parametric uncertainty (quantified on the short-term ensemble) through the proposed machine learning and analog ensemble approaches. Taken from Bodini et al. (2021).

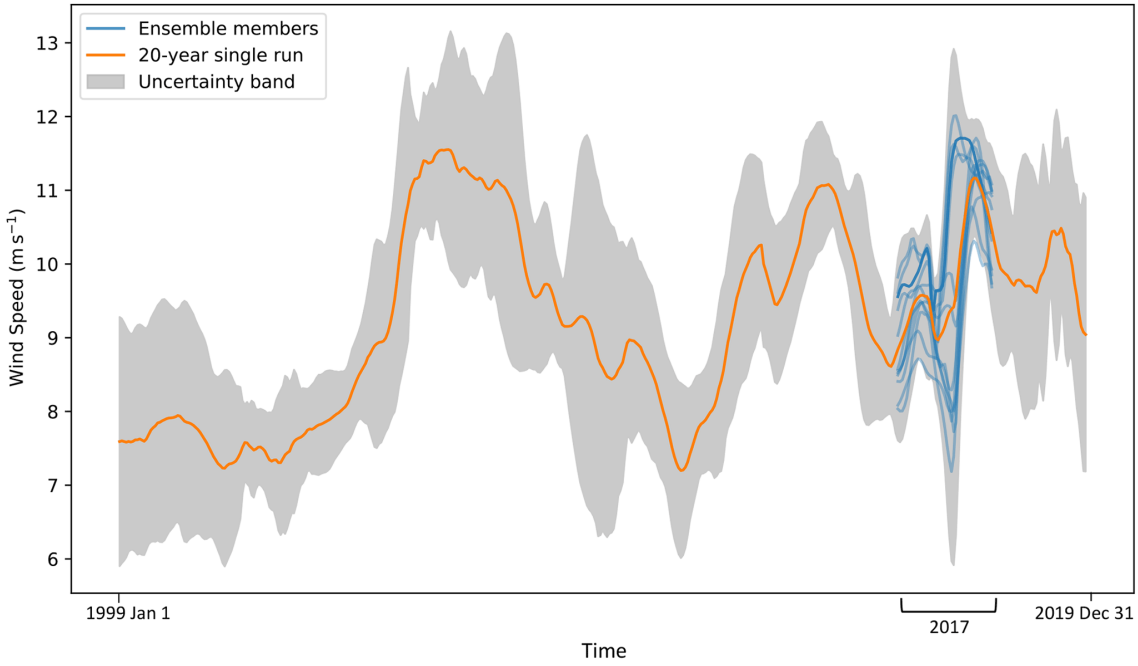

In the California OCS, we conducted tests using our proposed methods, utilizing the now deprecated MYNN-based 20-year simulation described in Optis et al. (2020a). The results indicated that both approaches accurately estimated the long-term wind speed boundary condition and parametric uncertainty, with an r^2 greater than 0.75. Comparatively, the gradient-boosting model performed slightly better than the analog ensemble. Additionally, we examined the physical variability in the uncertainty estimates and observed that wind speed uncertainty increases as proximity to land decreases. Furthermore, stable and unstable atmospheric conditions exhibited larger uncertainty compared to neutral conditions, and the winter season displayed a smaller boundary condition and parametric sensitivity in comparison to summer. Lastly, we present a median hourly uncertainty ranging from 10% to 14% of the average 100-m wind speed values across the offshore wind energy lease areas in the region (Figure 7).

Figure 7. Median hourly boundary condition and parametric uncertainty for the 100-m wind speed, as derived from the (a) machine learning approach, (b) analog ensemble, and (c) difference between the two. Taken from Bodini et al. (2021).

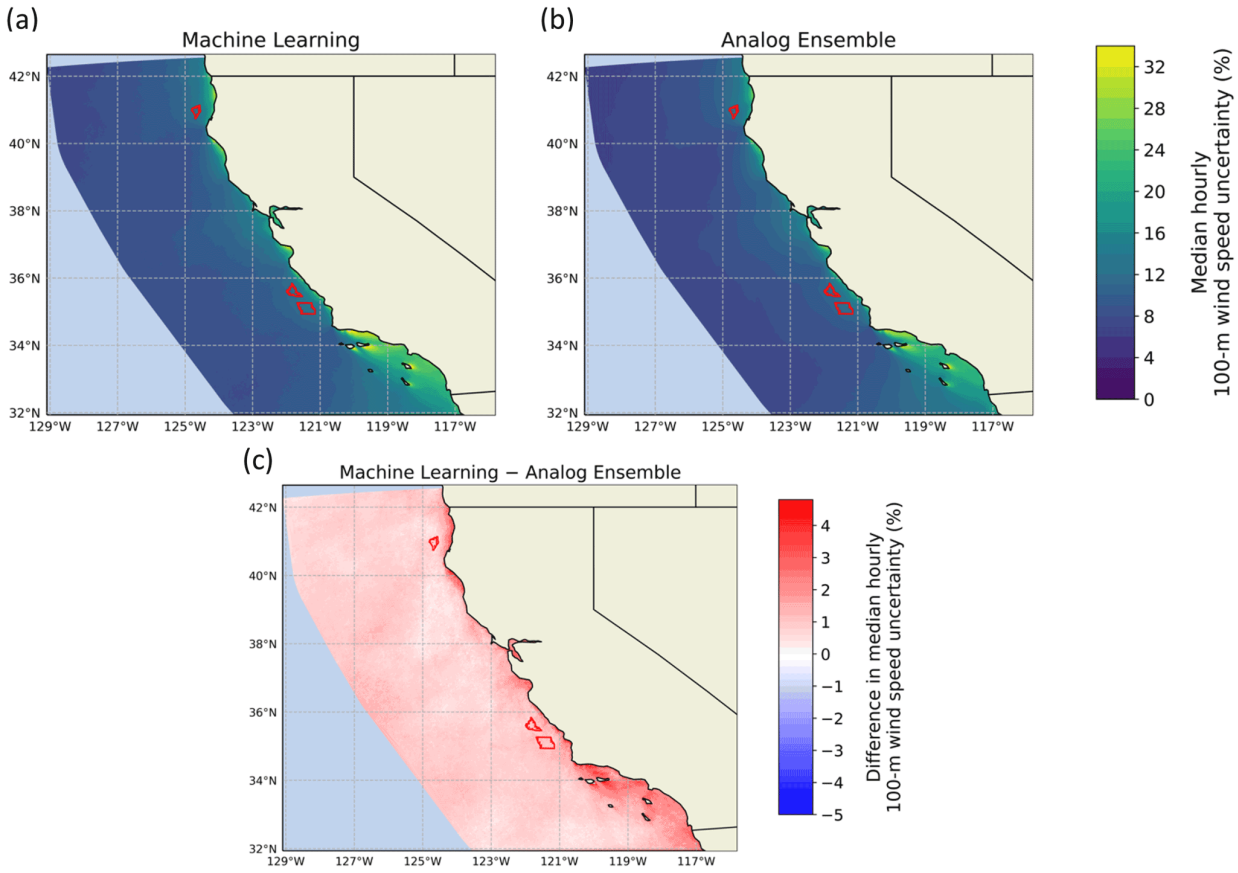

The results of this analysis are described in detail in Bodini et al. (2021).

3.3 Model uncertainty compared to observations

Although the assessment of boundary condition and parametric uncertainty is valuable in numerical modeling, it is subject to certain limitations. The magnitude of the quantified boundary condition and parametric uncertainty derived from the variability of the WRF ensemble is directly tied to the limited number of choices sampled within the considered model setups. As a result, only a portion of the actual wind speed error in relation to observations can be effectively quantified. To fully capture the uncertainty in wind speed predicted by NWP models, direct observations of the wind resource are necessary. In such cases, the residuals between the modeled and observed wind speeds can be calculated, enabling the quantification of model error in terms of both bias (i.e., the mean of the residuals) and uncertainty (i.e.,

the standard deviation of the residuals). The resulting model uncertainty would then be combined with the inherent uncertainty of the wind speed measurements.

We applied this approach in the Mid-Atlantic region. Given the lack of long-term hub-height offshore wind speed observations in the region, we developed a methodological framework to leverage both floating lidar and near-surface buoy observations to quantify uncertainty in the long-term modeled hub-height wind resource. To accomplish this, we trained and validated a machine learning regression model capable of vertically extrapolating near-surface wind speed to hub height, utilizing the available short-term lidar data sets in the region. Subsequently, we applied this trained model to extrapolate the long-term near-surface buoy wind speed observations to hub height, allowing for a direct comparison with the long-term numerical data set. Through this comprehensive approach, we discovered that the average 20-year uncertainty in 140-m wind speed across the region is slightly below 3 m s^{-1} (Figure 8). Notably, we found greater uncertainty in stable atmospheric conditions.

Figure 8. Map of long-term mean uncertainty (in m s^{-1}) in modeled 140-m hourly average wind speed at the locations of NDBC buoys (whose IDs are listed in the map legend) across the Mid-Atlantic domain.

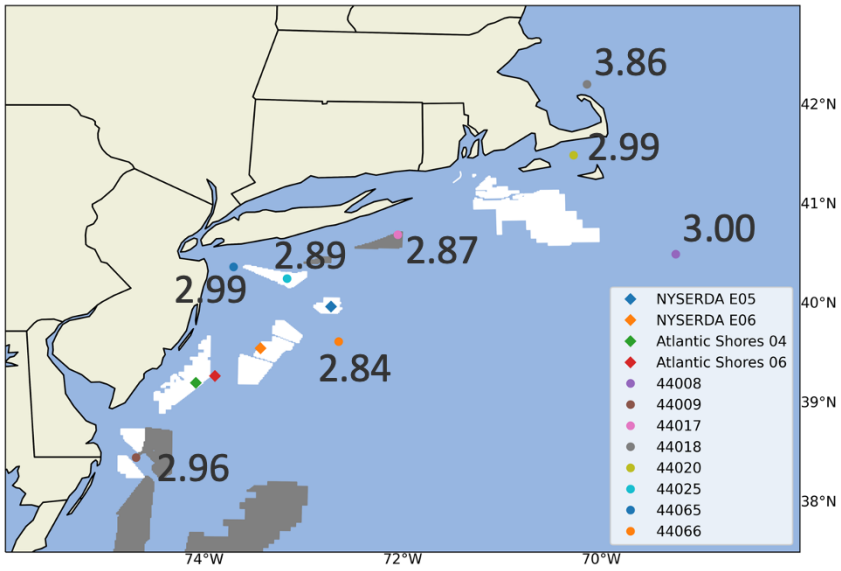

The results of this analysis are described in detail in Bodini, Castagneri, and Optis (2023).

4 A post-construction data set in the Mid-Atlantic region: NOW-WAKES

Offshore wind resources often exist in close proximity to densely populated areas, creating the potential for rapid wind plant development. However, wind turbines and wind plants produce wakes, which are regions characterized by reduced wind speeds that can negatively impact downstream turbines and plants. As part of the NOW-23 data set, we generated NOW-WAKES, a 1-year post-construction data set specifically to model and evaluate the effects of offshore wakes generated by upcoming wind plants in selected lease and call areas within the Mid-Atlantic region, as of 2019. In this analysis, we also explored the uncertainty associated with certain modeling choices by employing two different PBL schemes for these simulations. Here, we provide a brief summary of the two studies conducted and refer interested readers to our peer-reviewed journal articles on the subject for more comprehensive details (Rosencrans et al. in review; Rybchuk et al. 2022).

To assess wake variability and annual energy production, we conducted a yearlong series of simulations that involved three scenarios: simulations with no wind plants, simulations with a single wind plant, and simulations with complete build-out of the lease areas. We utilized the WRF model to calculate wake effects and distinguish between wakes generated within a single plant and those generated externally between different plants. The wind plant simulations incorporated 12-megawatt (MW) turbines at a density of 3.14 MW km^{-2}, matching the planned density of 3 MW km^{-2}. Our findings revealed that the most significant wakes, propagating up to 58 km (Figure 9), occurred during stable stratification in the summer, coinciding with peak grid demand in New England. The offshore region exhibited more substantial seasonal variability in wakes compared to diurnal variability. The average wake impacts throughout the year resulted in a 35.9% reduction in power output, with internal wakes causing more substantial power losses (27.4%) than external wakes (14.1%). To incorporate wake uncertainty, we introduced variations in the amount of added turbulence kinetic energy (TKE) from turbines, leading to a power output variability of 3.8%. Finally, we compared the annual energy production to the energy demand of the New England grid and found that the lease areas had the potential to supply approximately 60% of the annual load.

Figure 9. Mean wake wind speeds from the lease areas, for stable conditions, as seen in NOW-WAKES. The wind speed deficit is shown by the colored contour, and the turbines are shown as black dots. The 0.5 m s^{-1} deficit is shown by the dotted black line. Taken from Rosencrans et al. (in review).

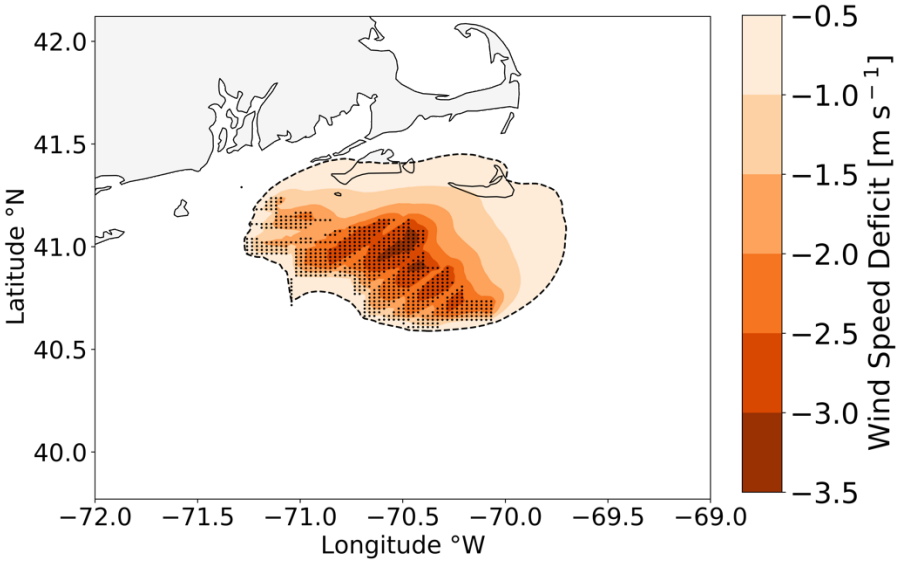

The results of this analysis are described in detail in Rosencrans et al. (in review).

It is important to note that different simulation methodologies can be utilized to estimate the impact of wind plant wakes in WRF. Each methodology possesses its own level of accuracy and sensitivity to input parameters. For instance, during the development of the NOW-23 data set, mesoscale simulations without turbines exhibited variations in hub-height wind speeds due to the chosen PBL scheme. However, the sensitivity of modeled wind plant wakes to different PBL schemes had not been explored previously, as wake parameterizations were solely compatible with the MYNN PBL scheme. To overcome this limitation, we combined the WRF Fitch wind farm parameterization (Fitch et al. 2012) with the newly introduced National Center for Atmospheric Research (NCAR) 3DPBL scheme (Kosović et al. 2020; Juliano et al. 2022) and compared the results against those obtained using the MYNN PBL scheme (Figure 10). To conduct this comparison, we simulated an idealized wind plant under stable, neutral, and unstable atmospheric conditions, ensuring matching hub-height wind speeds using both PBL schemes. The findings revealed differences in the average losses of hub-height wind speeds within the wind plant between the two PBL schemes, ranging from −0.20 to 0.22 m s^{-1}. Correspondingly, the capacity factors varied from 39.5% to 53.8%. These results indicate that the choice of the PBL scheme can contribute to the uncertainty in modeled wakes. Therefore, we strongly recommend incorporating PBL variability in wind plant planning sensitivity and forecasting studies to account for this additional source of uncertainty.

Figure 10. Mean wake wind speed deficit from the lease areas, for stable conditions, using the MYNN PBL scheme (left) and the NCAR 3DPBL scheme (right), at 138 m asl.

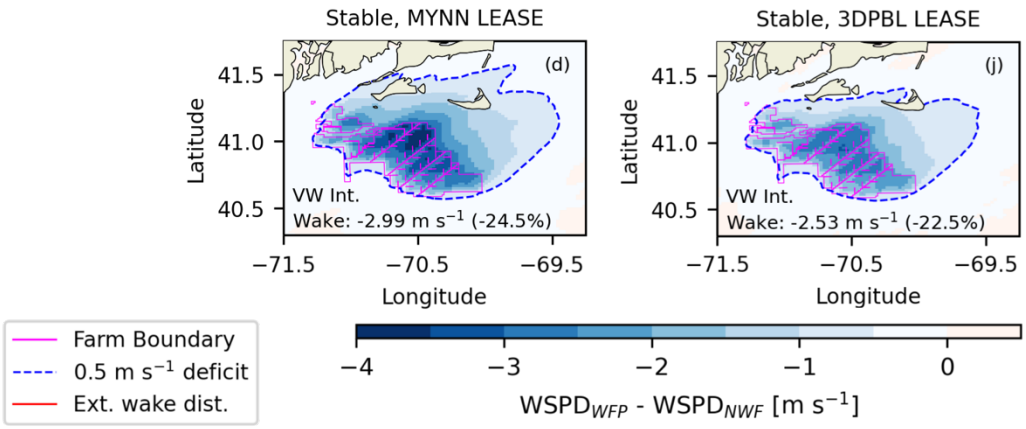

The results of this analysis are described in detail in Rybchuck et al. (2022).

5 Deriving offshore turbulence intensity from WRF

This part of the project was completed by the PNNL team. The analysis focused on three offshore regions: Mid-Atlantic, Gulf of Mexico, and South Pacific. For the Mid-Atlantic case, we provide here a summary and note that a more detailed analysis can be found in Tai et al. (in review).

5.1 Background

In wind energy applications, atmospheric turbulence is often quantified by using the turbulence intensity (TI), which is also the primary input for standard wind turbine design. Accurately characterizing the spatiotemporal variability of TI should lead to improved predictions of power production. Earlier studies, including Kaiser et al. (2007), Clifton and Wagner (2014), Bardal and Sætran (2017), and Saint-Drenan et al. (2020), and have discussed how TI may influence power production of turbines. It has been shown that the power production during periods of high or low TI can vary by up to 20% (Clifton and Lundqust 2012). Nonetheless, there have been fewer turbulence measurements over the ocean than over land due to difficulties in instrument maintenance and operation over the open ocean for long durations.

Atmospheric models such as NWP models and large-eddy simulation models can potentially mitigate this problem, as they can simulate turbulence based on atmospheric and surface conditions in any region over the globe. While large-eddy simulation models are too computationally expensive to simulate long periods of time, mesoscale model simulations are much more affordable and can estimate turbulent properties such as TKE by applying an applicable turbulence parameterization. However, despite the applicability, TI derivation from mesoscale models has rarely been mentioned in previous studies. To address this shortcoming, we implement TI derivations in the standard version of the WRF and validate them in the offshore environment.

Since the nature of atmospheric turbulence is a function of the sea-air temperature difference and atmospheric stability, the model representation of SST is a critical component for an accurate turbulence prediction. SST serves as the lower boundary conditions over the ocean grids in the atmospheric model, and it is one of the known uncertainties in simulating near-surface atmospheric turbulence in the offshore environment (Redfern et al. 2023). Due to insufficient coverage of sea surface temperature observations over the ocean, it has been challenging to obtain realistic representation of fine-scale SST features. Earlier studies found the evolving SST spatial gradients could have notable impact on the heterogeneity of atmospheric states within the marine atmospheric boundary layer through heat fluxes in the sea-air interface (Sullivan et al. 2020). Hence, it is necessary to introduce high-resolution SST forcing into the

model to drive atmospheric models. We explore the impact of SST forcing on simulated TI by incorporating high-resolution SST in the simulations. The overall model performance with respect to wind and turbulence is accessed using Doppler lidar observations collected near the mid-Atlantic, California, and Gulf of Mexico coasts in the United States.

5.2 Observational data

5.2.1 Mid-Atlantic

The observations were collected during a field campaign the was conducted from February to June 2020 near the Woods Hole Oceanographic Institution's Martha's Vineyard Coastal Observatory (MVCO) with the goal of evaluating the performance of one of DOE's lidar buoys. The MVCO is a purpose-built facility for conducting detailed atmospheric and oceanic research. A major component of the MVCO is the Air-Sea Interaction Tower (ASIT, Figure 11). At ASIT, a suite of wind measurement devices were installed, including a pair of cup anemometers at the top of the tower (26 m asl), a wind vane at 23 m asl, and a WindCube V2 vertically profiling lidar on the main platform at 13 m asl. The lidar measurements, including wind speed and TI, are obtained at 10 heights: 53, 60, 80, 90, 100, 120, 140, 160, 180, and 200 m asl. Moreover, the meteorological and sea surface conditions were collected by the ASIT and a buoy and are used to determine the local atmospheric stability.

Figure 11. Map depicting the WRF model domain used for the simulations in the Mid-Atlantic region. The red star denotes the location of the MVCO ASIT. Color shading represents the terrain height in kilometers.

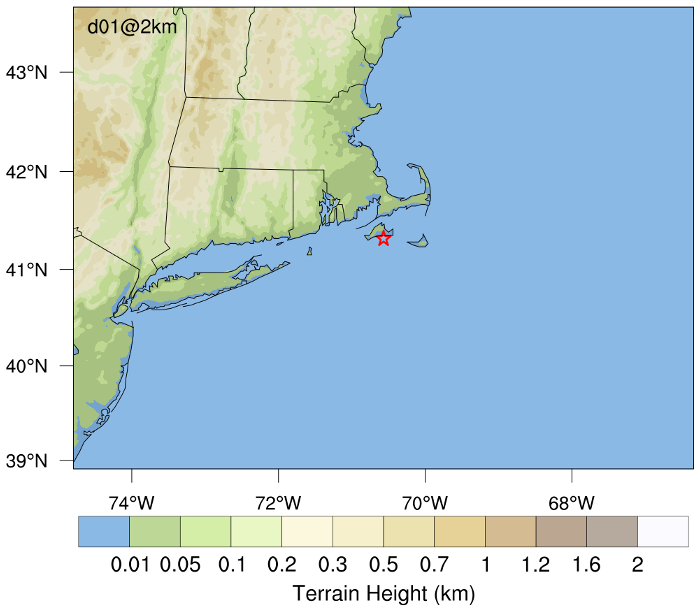

5.2.2 California coast

Two offshore lidar buoys managed by PNNL were deployed off the coast of California (Figure 12). The period of the deployments was from mid-October 2020 to late June 2021. One buoy was sited in water approximately 625 m deep off Humboldt County along the northern California coast (40.97°N, 124.59°W). Another buoy was deployed in water about 1,000 m deep off Morro Bay along the central California coastline (35.71°N, 121.87°W).

The two lidar buoys collect a comprehensive set of meteorological and oceanographic measurements needed for offshore wind resource characterization. The centerpiece of the instrumentation on each buoy is a motion-corrected lidar system that provides profiles of the wind speed and direction up to 250 m asl. In addition to the lidars, each buoy collects complementary oceanographic and near-surface meteorological data, such as ocean current profiles, air humidity and temperature, and sea temperature.

Figure 12. (a) Map depicting the locations of the two DOE lidar buoys deployed off the California coast near Humboldt and Morro Bay. Two overlaid boxes display geographical coverage of the two model domains that correspond to panels (b) and (c). Contours in (b) and (c) represent terrain height in meters asl.

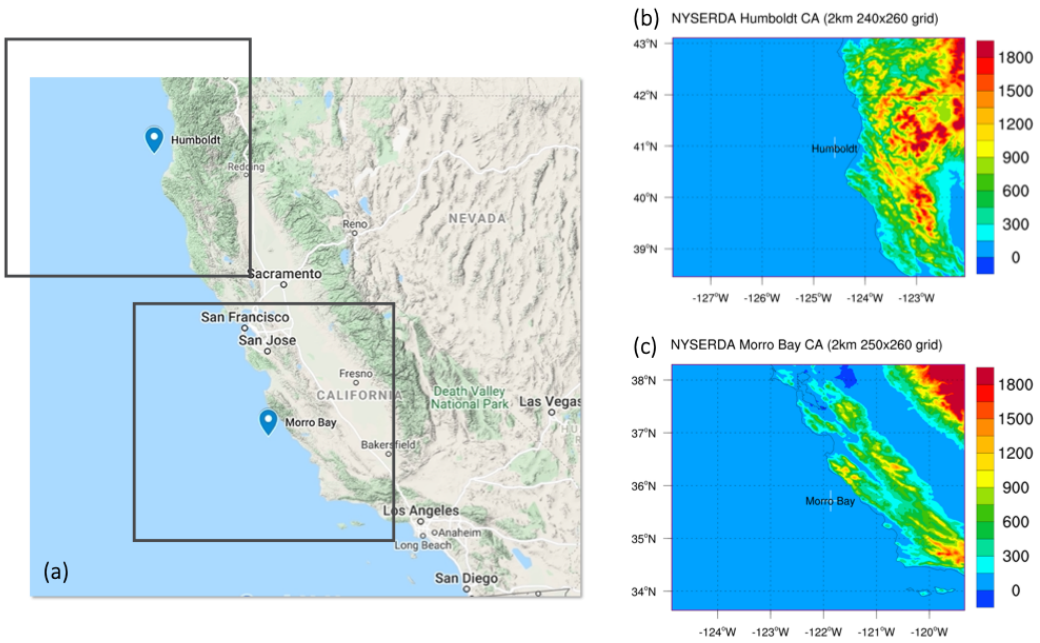

5.2.3 Gulf of Mexico

The Shell Exploration and Production Corporation has been operating a network of gas and oil platforms in the north and central regions of the Gulf of Mexico. On these platforms, numerous meteorological and

oceanographic instruments, including lidar wind profilers, are deployed to provide local weather and oceanic information. We use the observations from two lidar wind profilers for model evaluation (Figure 13). The first lidar wind profiler is mounted on the tension-leg platform (TLP) Ursa (28.2°N, 89.12°W; ~54 m asl) and has been measuring vertical profiles of wind speed and direction since 2017. The lidar obtains approximately 50 measurements during each 1-second scan. By combining those observations, the wind vectors at specific height levels above the lidar (10, 20, 38, 40, 50, 60, 70, 80, 90, and 100 m) were obtained. The other lidar is deployed on the TLP Mars (28.16°N, 89.22°W; ~55 m asl), and data were recorded at 15, 25, 35, 38, 45, 55, 65, 75, 85, 90, 105 m above the lidar, from September 2017 to January 2023.

Figure 13. Map depicting the WRF model domain used for the simulations in the Gulf of Mexico. The locations of two Shell gas and oil platforms (Ursa and Mars) are denoted by red and yellow dots.

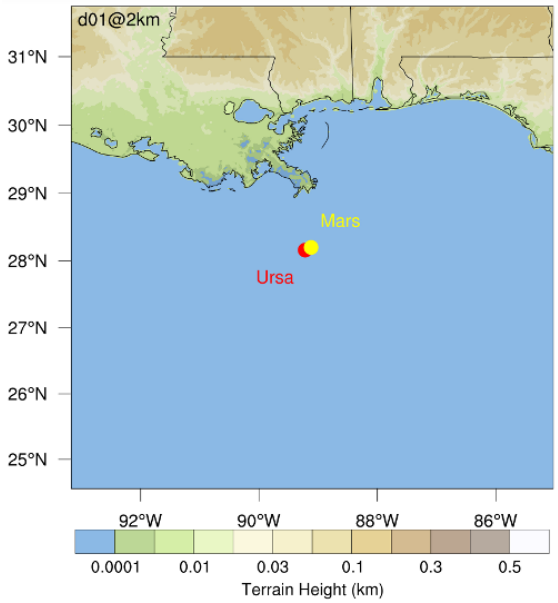

5.3 Methodology

5.3.1 Derivation of TI in WRF model and implementation

TI is defined as the standard deviation of the horizontal wind speed (σ_U) divided by the average horizontal wind speed over a time interval ($\overline{U}$):

$$TI = \frac{\sigma_U}{\overline{U}}, \qquad with \;\; U = \sqrt{(u^2 + v^2)} \tag{1}$$

Horizontal wind vectors (u and v) from the lidar were calculated at ~1 Hz using the raw radial velocity measurements along the cardinal directions. Although the winds are reconstructed at 1 Hz, the winds are a combined product of a trailing ~4 seconds of sampled radial velocity measurements. The reconstructed 1-Hz horizontal wind speed measurements are used to calculate TI from the Doppler lidar, as shown in the preceding equation over 10 minutes.

On the other hand, TKE is generally estimated as

$$TKE = \frac{1}{2}(\sigma_u^2 + \sigma_v^2 + \sigma_w^2) \quad (2)$$

where σ_u^2, σ_v^2, and σ_w^2 are the variances of zonal, meridional, and vertical wind components, respectively. For 10-minute averaged TKE from reference lidar profilers, horizontal velocity variance was estimated using the 1-Hz u and v components of velocity, and the vertical velocity variance was estimated using the lidar central beam staring vertically up (like Arthur et al. 2022).

Realistically, observed TI occurs across a range of spatial and temporal scales. The application of the WRF model leads to an artificial separation of motions that are explicitly represented by the model and turbulence treated by the turbulence parameterization; thus, both grid-resolved and sub-grid motions can give rise to TI. These two contributions to TI are referred to as model-resolved TI and sub-grid TI, respectively.

Here, a new algorithm is implemented in WRF to extract the wind variation and mean wind speed over a 10-minute window, allowing for the calculation of both sub-grid and model-resolved TI. Since the three-dimensional components of turbulent wind speed cannot be obtained through the boundary layer parameterization, the sub-grid TI is derived by leveraging TKE prognosed by the MYNN boundary layer parameterization. The TI formula for deriving sub-grid TI is also used in earlier studies such as Shaw et al. (1974), Wharton and Lundquist (2011), and Bodini, Lundquist, and Kirincich (2020):

$$TI = \frac{\sqrt{\sigma_u^2 + \sigma_v^2}}{\overline{U}} \quad (3)$$

Our observational analysis using the lidar-measured wind variances collected at the MVCO ASIT over a 6-month period indicates that σ_w^2 (variance of vertical wind) is generally much smaller than σ_u^2 and σ_v^2 (Figure 14a) regardless of stability (Figure 14b). In most conditions, the fraction of σ_w^2 in total wind

variance ($\frac{\sigma_w^2}{\sigma_u^2+\sigma_v^2+\sigma_w^2}$) is no greater than 0.2 (not shown). Therefore, the previous equation is approximated by the form of

$$TI = \frac{\sqrt{2 \cdot TKE}}{\overline{U}} \quad (4)$$

Figure 14. The lidar-measured wind variances collected at the MVCO ASIT from January to mid-June in 2020. The data are displayed (a) in the format of power density and (b) as a function of air-sea temperature difference (atmospheric stability).

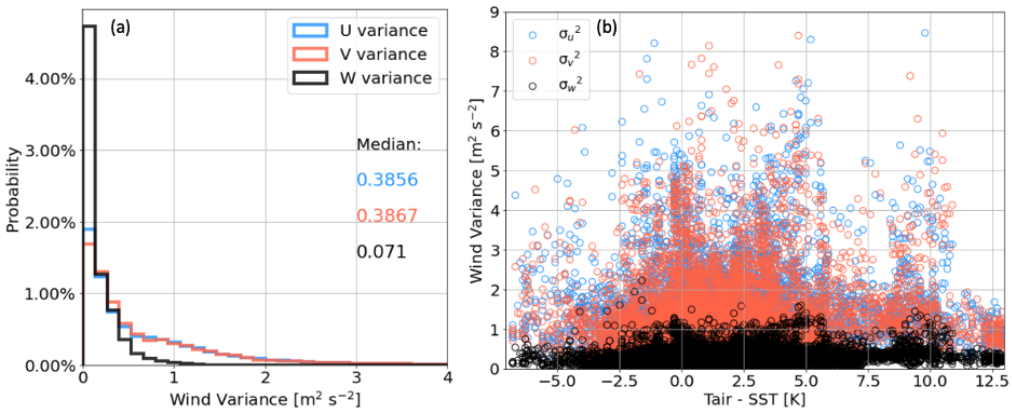

The instantaneous sub-grid TI can then be output at any model time step. A new variable was added to store the sub-grid TI and to have values written to the WRF model output files. In addition, the model was also modified to compute the model-resolved TI by adding calculations of running means and variances of the horizontal velocity components (zonal and meridional) within 10-minute windows that are then used to compute and output the resolved TI. A summary of the two components of TI from the WRF model is given in Table 4.

Table 4. Summary of comparison between two types of TI output from WRF model.

	Sub-grid TI	Model-resolved TI
Dynamic scale	Turbulence	Mesoscale wind fluctuations
Solution in model	PBL scheme (MYNN)	Resolved wind components
$\sqrt{\sigma_u^2 + \sigma_v^2}$	TKE (assume σ_w^2 is negligible)	Variance of u, v in 10-min window
$\overline{U}$	Mean horizontal wind speed in 10-min window	Mean horizontal wind speed in 10-min window

5.3.2 Model configuration

Version 4.2 of the WRF model is configured with a single domain to simulate offshore near-surface winds over three offshore regions (Figure 11, Figure 12, and Figure 13). Optis et al. (2020a) conducted a series of model sensitivity experiments with respect to surface layer and PBL parameterizations, reanalysis data, and SST forcing. The results of their model assessment indicated that the largest uncertainty is associated with the choice PBL parameterizations, and the MYNN boundary layer parameterization (Nakanishi and Niino 2009) generally outperforms the YSU (Hong, Noh, and Dudhia 2006) scheme off the U.S. East Coast. Hence, the MYNN boundary layer parameterization, as well as other parameterizations described by Optis et al. (2020a), are used in most of our simulations. We noticed some errors in our WRF simulations along the West Coast, and also conducted some experiments with the YSU parameterization to examine the model sensitivity.

Our simulations use a horizontal grid spacing of 2 km and a stretched vertical coordinate of 60 levels (approximately 10 model levels between the surface and 200 m). The Eta (Ferrier) microphysics parameterization, MYNN surface layer parameterization, Unified Noah land-surface parameterization (Chen and Dudhia 2001), and the Rapid Radiative Transfer Model for global climate model applications longwave and shortwave radiation parameterization (Iacono et al. 2008) are employed to handle the corresponding physics. Initial and boundary conditions are taken from the National Oceanic and Atmospheric Administration's High-Resolution Rapid Refresh (HRRR; Benjamin et al. 2016) product. The HRRR analysis has several advantages over other coarse-resolution reanalysis products. For instance, 1) the model core of HRRR, the WRF model, is identical with what we use in this study; 2) it has a grid spacing of 3 km, which is very close to the grid spacing used here (2 km); and 3) it is constrained hourly by assimilating radar observations including Doppler velocity and reflectivity, which reduces the uncertainties in the prediction of precipitating clouds. All these advantages would primarily mitigate model uncertainties in part due to issues in model balance and spin-up.

5.3.3 SST sensitivity experiment

Since the near-surface atmospheric stability may strongly influence turbulence intensity at hub height, the uncertainty in representation of sea surface temperature should also be considered. Although HRRR analysis better represents convective-scale structures than other coarse-resolution reanalysis products do, it does not provide corresponding SST forcing data. The "baseline" experiment uses the climatological SST provided with WRF as its SST forcing and is a concatenation of a series of 36-hour simulations. Each of these simulations is initialized at 00 UTC and continuously integrated for 36 hours. To avoid

model spin-up issues, the first 12 hours of each simulation are discarded, and the resulting 24 hours of results are retained for the analysis.

On the other hand, a sensitivity experiment (named *sstupdate* hereafter) is also conducted to examine the variability induced by replacing the SST forcing in the model. Note that the main NOW-23 analysis used two SST products: the OSTIA data set (Donlon et al. 2012) and the NCEP RTG SST product (National Weather Service 2014). Here, we use the NASA Jet Propulsion Laboratory Level 4 MUR Global Foundation Sea Surface Temperature Analysis (V4.1; Chin, Vazquez-Cuervo, and Armstrong 2017), which has an even higher spatial resolution than either the OSTIA or NCEP RTG. The SST analysis product assimilates satellite data with a range of resolutions, including the Moderate Resolution Imaging Spectroradiometer infrared (1 km), Advanced Very High Resolution Radiometer infrared (5–9 km), microwave (25 km) and in situ measurements (pointwise). The Multi-Resolution Variational Analysis technique is employed to reconstruct fast-moving fine-scale features as well as fill the large-scale data void.

5.4 Results

5.4.1 Mid-Atlantic

5.4.1.1 Near-sea-surface wind, turbulence, and sea-air temperature gradient

The simulated wind speed, wind direction, TI, TKE, and sea-air temperature gradient (air temperature at 2 m asl minus SST) are compared against data measured by a tower-mounted lidar and a buoy deployed at the MVCO ASIT. Here, the sea-air temperature gradient is considered as a proxy of atmospheric stability near the sea surface. Thus, negative values indicate unstable (convective) conditions, whereas stable conditions are likely when the temperature gradient is positive.

The results for March 2020 are given as an example in Figure 15. The model generally reproduces most of the "convective" (negative values of T_{air} − SST; red patches) events in the period. While simulated TKE is generally smaller than observed TKE, both observations and simulations show larger TI and TKE during convective periods, indicating that the model's PBL scheme reacts reasonably well in response to the varied lower boundary conditions. During stable periods (positive values of T_{air} − SST; blue patches), simulated TKE and TI decrease dramatically with height. This indicates weak turbulence-limited vertical mixing in these cases.

Figure 15. Time-height comparison of wind speed (WSPD), wind direction (WDIR), air-sea temperature gradient (T_{air} − SST), turbulence kinetic energy (TKE), and sub-grid turbulence intensity (TI). Results for lidar and buoy observations and "baseline" simulation during the period of March 2020 are given in (a) and (b), respectively.

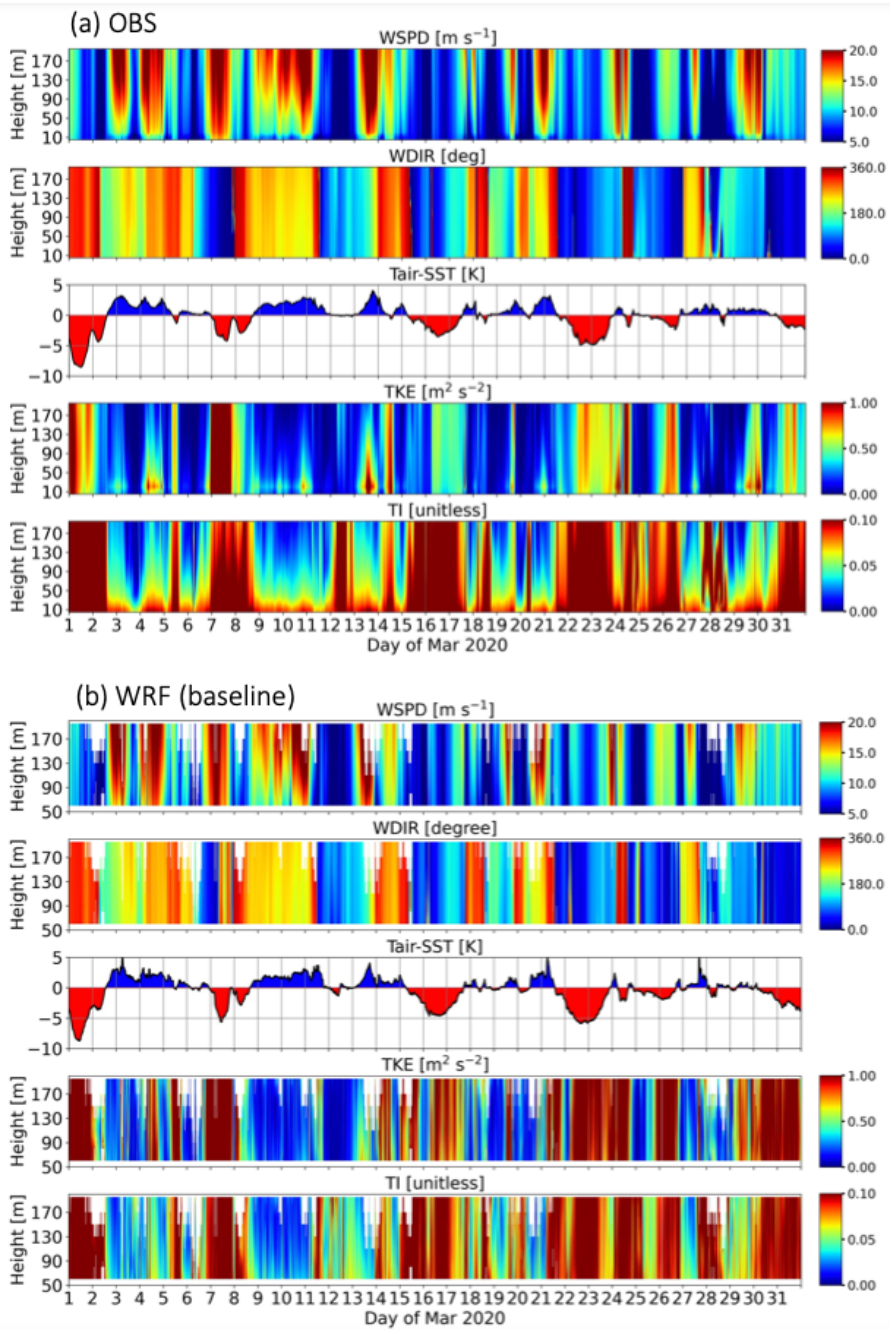

To quantify the model performance for the entire period of study, an assessment of the baseline simulation is carried out that examines the 80-m TI, TKE, wind speed, and air-sea temperature gradients. Note that data points from simulations and observations are only counted when wind speed is between 5 m s^{-1} and 25 m s^{-1}, which is consistent with turbine cut-in and cut-out wind speeds of typical commercial

wind turbines. Three metrics, including root mean square error, bias, and correlation coefficient, are computed for each variable and given in Table 5.

Overall, the WRF model slightly underestimates TI with a bias of −0.0061 (~5% relative to mean value) and has a RMSE of 0.037 (~30% relative to mean value). The two main factors in the computation of TI, TKE and wind speed, exhibit notable contrasts in their assessments. While simulated TKE is underpredicted with a bias of −0.3804 $m^2 s^{-2}$ and RMSE of 0.914 $m^2 s^{-2}$, wind speed generally agrees well with lidar observation, as demonstrated by the relatively larger correlation coefficient (0.83) in comparison to 0.74 for TKE. This implies that the errors in TI are more likely driven by the biases in TKE. Lastly, the air-sea temperature gradient is reasonably represented with the highest correlation coefficient among all the variables of 0.92.

Table 5. Metrics, including correlation coefficient, root mean square error (RMSE), and bias, of 80-m TI, TKE, wind speed, and air-sea temperature difference are given as computed for baseline and *sstupdate* simulations.

	TI		TKE		Wind speed		T_{air} − SST	
	baseline	sstupdate	baseline	sstupdate	baseline	sstupdate	baseline	sstupdate
r^2	0.56	0.59	0.74	0.74	0.83	0.84	0.92	0.94
RMSE	0.037	0.035	0.914	0.886	2.37	2.303	0.921	0.766
Bias	−0.0061	−0.0023	−0.3804	−0.3526	0.3737	0.3165	0.3223	0.093

5.4.1.2 Sensitivity to SST forcing

Results from the *sstupdate* simulation indicate that the replacement of SST forcing has positive impacts on all the examined variables (Table 5). For instance, the r^2, RMSE, and Bias for TI as simulated by *sstupdate* (baseline) are 0.59 (0.56), 0.035 (0.037), and −0.0023 (−0.0061). Similarly, the model skill improves simultaneously with respect to TKE, wind speed, and T_{air} − SST, suggesting that a more realistic SST forcing helps better represent stability and subsequently the surface fluxes. This then influences turbulent properties within the boundary layer, such as the TKE and wind speed.

The probability density functions (PDFs) are given to help contrast the three data sets (Figure 16). Figure 16a shows that the distribution of observed TI has a wider peak between 0.025 and 0.1 than the simulated distributions. While the baseline simulation has more points with smaller TI values (peak ~0.04), the distributions of TI from the *sstupdate* show an additional peak around 0.09 and 0.1, and there are more large values of TI. The median TI of *sstupdate* (0.066) is much closer to the observations (0.07) than the baseline (0.057), indicating that the SST representation has a notable impact on the TI simulation. The

impacts of SST on TKE, wind speed, and air-sea temperature difference is displayed in Figure 16b, c, and d, respectively. The model tends to produce more instances with smaller TKE than the observed TKE (0.67 m^2 s^{-2}), and *sstupdate* (0.4 m^2 s^{-2}) has slightly larger median TKE than the baseline (0.377 m^2 s^{-2}). Note that it was shown that part of the discrepancy in TKE may be attributed to varying uncertainty in lidar turbulence retrievals as a function of atmospheric stability (Sathe et al. 2015). The wind speed comparison (Figure 16c) indicates that while both simulations have relatively larger medians (10.94 m s^{-1} and 10.86 m s^{-1}) than the observations (10.31 m s^{-1}), the high-resolution SST used in *sstupdate* slightly improves the simulations. The overall improvement in wind speed can be related to more accurate representation of stability, as the PDF of simulated air-sea temperature gradient is improved accordingly when applying the high-resolution SST forcing (Figure 16d).

Figure 16. Probability density function plots illustrating the results of (a) sub-grid turbulence intensity, (b) turbulence kinetic energy, (c) wind speed, and (d) air-sea temperature difference among baseline, *sstupdate* simulations, and observations at hub height (~80 m) in February to May of 2020. The median of each data set is given in each panel with color coding.

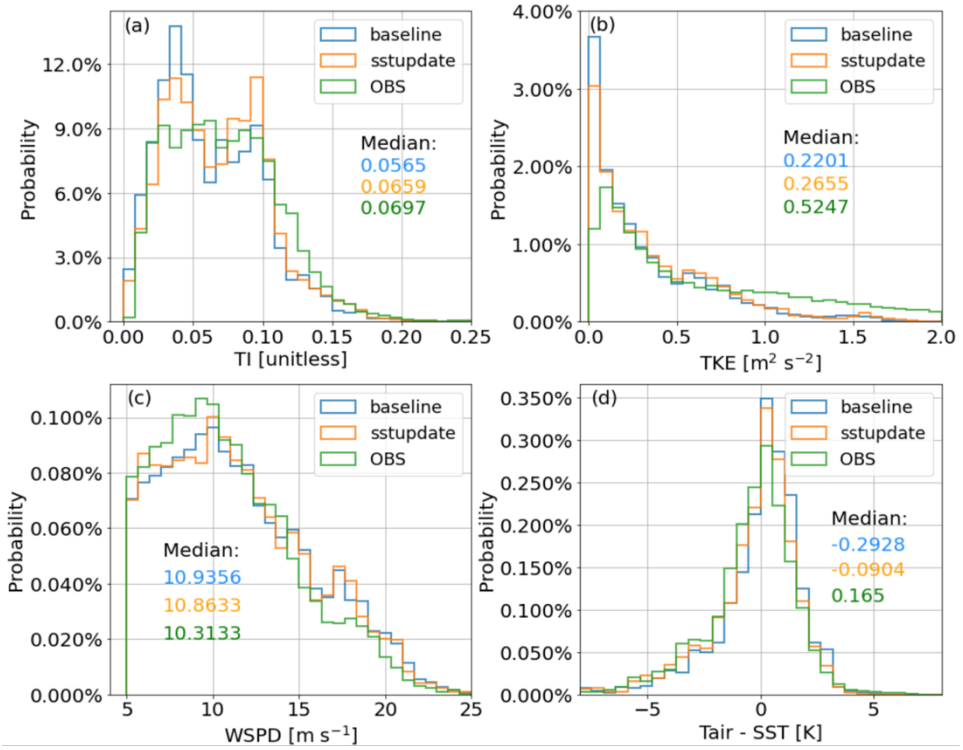

The impact of SST is also examined by monthly variability. Figure 17 summarizes the monthly variation of metrics as calculated for both the baseline and *sstupdate* simulations. The analysis suggests that the overall model skill in air-sea temperature gradient is improved when introducing higher-resolution SST forcing, and the improvement is more distinct in the spring months than in February. Despite the

relatively small impact on the correlation for simulated air-sea temperature gradients (Figure 17a), the corresponding RMSE (Figure 17b) and bias (Figure 17c) for air-sea temperature gradients are considerably reduced. While relatively little positive impact is shown for TKE and wind speed, the improvement of TI is prominent, as indicated by the reduced RMSE and bias.

Figure 17. Monthly variation of (a) correlation coefficient, (b) root mean square error, and (c) bias for variables TI, wind speed, TKE, and air-sea temperature gradient from February to May in 2020. The solid line with circles represents baseline result. The dashed triangle line depicts the corresponding values from *sstupdate* simulation.

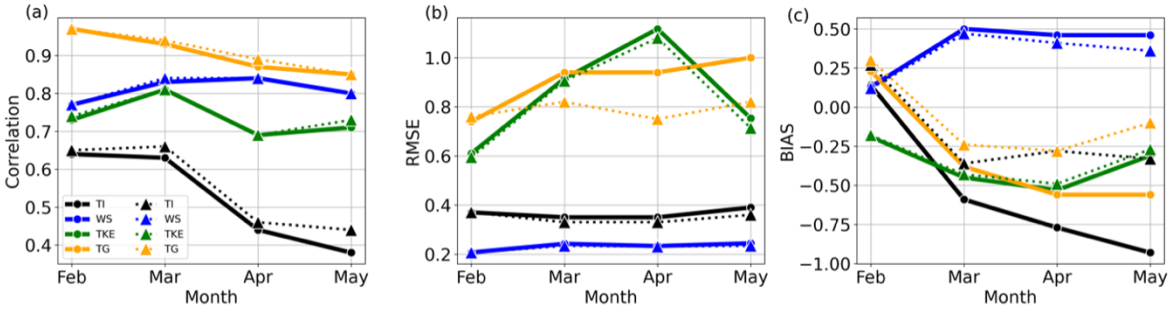

5.4.1.3 Relationship between turbulence intensity and bulk Richardson number

The bulk Richardson number (Ri_b) has been considered as a good indicator for turbulent conditions and flow transitions between turbulence and laminar states because it considers stability associated with the temperature gradient as well as the relative contributions of buoyancy and shear (e.g., Rodrigo et al. 2015; Bardal et al. 2018; Hsu 1989; Zoumakis and Kelessis 1991; Hansen et al. 2012). The equation we use for calculating the Ri_b is

$$Ri_b = \frac{g\Delta\theta_v \Delta z}{\overline{\theta_v}(\Delta u^2 + \Delta u^2)} \quad (5)$$

where g denotes gravitational acceleration, $\overline{\theta_v}$ is virtual potential temperature difference across a vertical layer of thickness z, and Δu and Δv represent the vertical gradient in horizontal wind components. The virtual potential temperature gradient ($\Delta\theta v$) is computed by using the air temperature (at 4 m) and sea surface temperature measurements on the buoy. The vertical gradients of horizontal wind components (u and v) are obtained by using wind measurements at 100 m from the Doppler lidar and 4 m from the buoy. We also applied a similar approach using the WRF model output. Note, the wind and temperature gradients are not computed from the same heights, and the bulk Richardson number calculated here will only be used to inform stability qualitatively (Howland et al. 2020). As for consistency, data for cases

where the wind speed was less than 5 m s^{-1} and greater than 25 m s^{-1} have been removed as described earlier. Figure 18 highlights the computed Rib during February 2020. It shows how both experiments reproduce the occurrence of observed unstable events (large negative Rib values). For instance, on February 14–15, 19–20, and 21, the model was able to produce large TI (over 0.2, Figure 18d) when Rib approaches −10 (Figure 18a).

While simulated results suggest that the model has good skill for large TI (over 0.2) events, there are periods of moderate TI (0.05 to 0.2) where the model fails to simulate observed peaks, as indicated by the green arrows in Figure 18d. It is found in those periods that the buoyancy component ($\Delta\theta v$) is mostly near zero (neutral conditions) or even positive (stable), whereas the shear component ($\Delta u^2 + \Delta u^2$) could be more variable from time to time, indicating how the model may have less skill in TI prediction when the buoyant forcing is relatively weak.

Figure 18. Time series of observed and simulated (a) bulk Richardson number, (b) shear component (m^2 s^{-2}), (c) buoyancy component (K), and (d) sub-grid TI during February 2020. Green arrows in (d) indicate events with large contrast in TI between model and observation. Filtered data points of sub-grid TI by using the thresholds of buoyancy > 0 K, shear < 20.0 m^2 s^{-2}, and TI > 0.06 are denoted in (e). Green line represents the model-resolved TI.

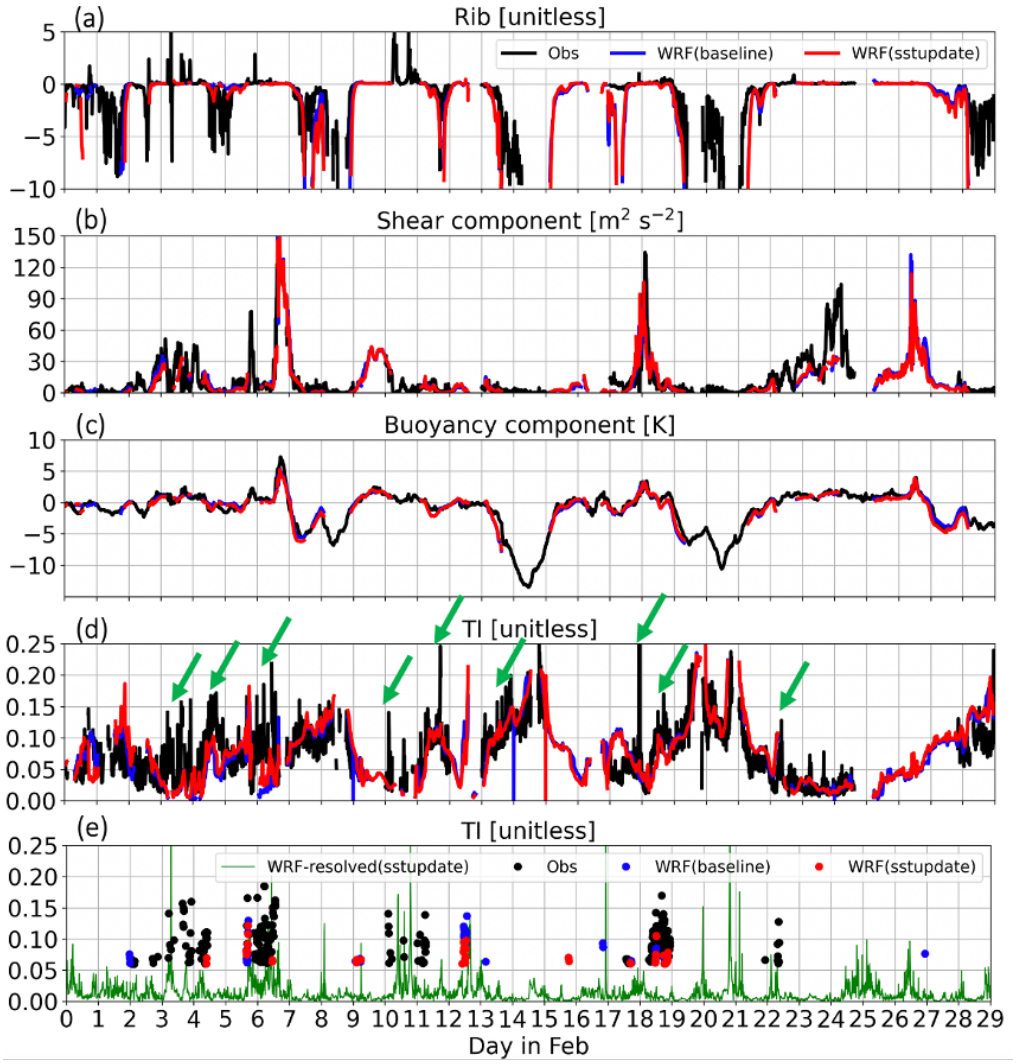

We map TI with respect to the buoyancy and shear components of Rib and show results in Figure 19. Figure 19a shows that the observed TI is generally larger during periods when conditions are unstable with a large and negative buoyancy component (SST is larger than air temperature). This implies that in convective regimes (buoyancy component < 0), more vigorous turbulence leads to stronger vertical mixing, which significantly reduces the wind shear. On the other hand, in stable regimes (buoyancy component > 0), less turbulent mixing often results in larger values of wind shear.

Although TI generally decreases as the buoyancy becomes more positive and the atmosphere becomes stable, as identified in the observations and the two WRF model configurations (Figure 19 a, b, and c), a population of reddish circles (large values of TI) in the lower-right quadrant of the figure does not follow this relationship (Figure 19a). While both simulations fail to represent these cases (Figure 19b and c), the fractional difference of simulated TI between the two simulations indicates that the sstupdate simulation generally has larger TI than the baseline simulation (Figure 19d). This can be attributed to an overall reduction of cold bias in the baseline simulation. Furthermore, a larger fractional increase of TI is found in the regime where the conditions are between neutral and slightly stable (buoyancy component ≥ 0). This is due to the weak negative temperature gradient in the baseline simulation becoming positive after replacing the SST forcing. Despite the correction, large TI is rarely simulated in the lower-right regime. This result is not surprising, as the formulation in the MYNN parameterization does not allow large values of TKE to be diagnosed in stable conditions.

We locate these specific data points in time by applying thresholds of buoyancy component > 0 K, shear component < 20.0 $m^2 s^{-2}$, and TI > 0.06 (black dashed-line box in Figure 19a). It shows that features leading to the large values of TI in the observation and simulations may not overlap in time, as the model may fail to simulate realistic conditions. Nevertheless, it is found that many of these cases with a positive buoyancy component and large TI are aligned with periods that have notable differences between observed and simulated TI, as denoted by green arrows in Figure 18d. Therefore, we conclude that the underrepresentation of this regime is likely responsible for most of the model bias in TI.

Figure 19. Scatter plots mapping the hub-height sub-grid TI in the coordinates of buoyancy and shear components for the entire period of study. Results of (a) observation (OBS), (b) baseline simulation, (c) *sstupdate* simulation, and (d) percentage of fractional difference (%) between *sstupdate* and baseline simulations are displayed. The black dashed-line box in (a) indicates the regime that is used to extract the data points as shown in Figure 18e.

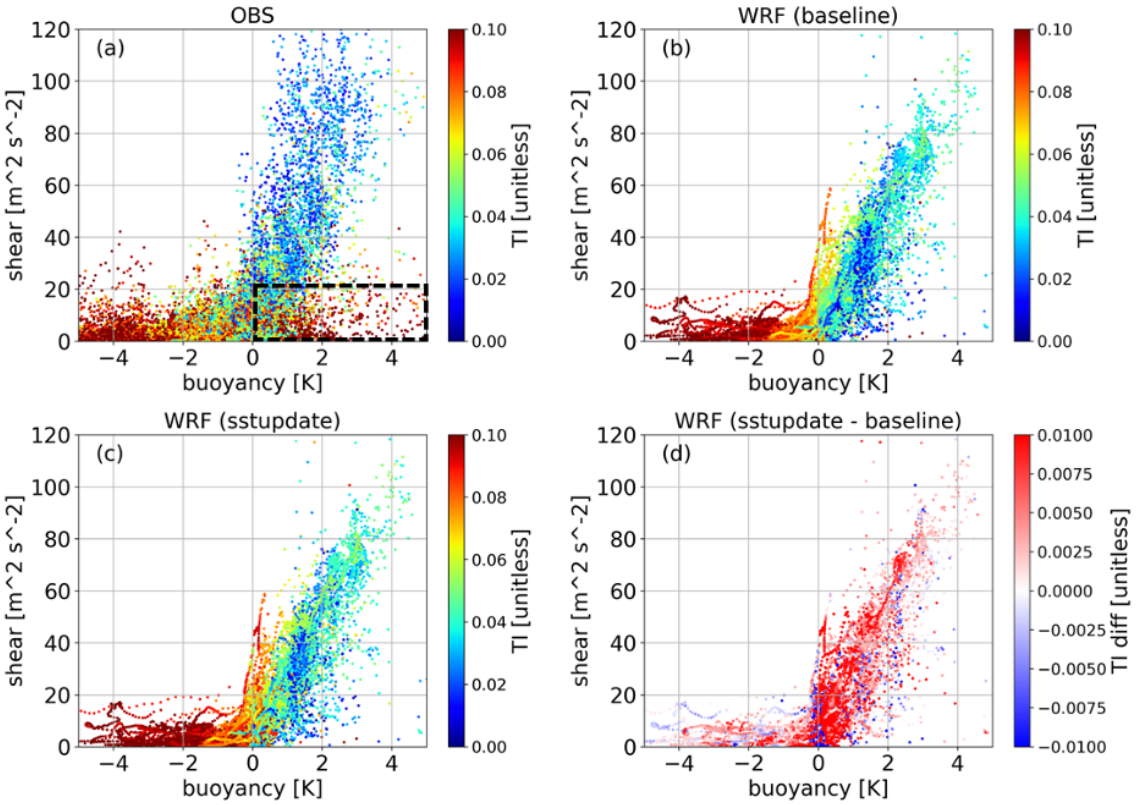

While some of the intermittent turbulent events may cause the occurrence of large TI under small shear and stable conditions, we find that most of the cases with large amounts of TI in stable conditions and weak shear can be linked to fluctuations in wind speed associated with mesoscale features of the flow and they are partially resolved by the mesoscale model. In Figure 18e, the model-resolved TI is denoted by the green line. For periods such as Feb. 3–4, 6–7, and 10–11, when the simulated sub-grid TI is much smaller than the observations, spikes in model-resolved TI have amplitudes similar to the observed values. This suggests the need to consider both sub-grid and model-resolved TI when modeling TI derived from a mesoscale atmospheric model. Furthermore, the uncertainties in the timing of simulated mesoscale weather events may lead to notable contrasts between the timing of modeled and observed peaks in TI. This can impact the simulated TI in two ways, as the mesoscale activity not only generates variance in the winds over larger spatiotemporal scales than the sub-grid turbulence but also effectively offsets dynamic and thermodynamic conditions near the sea surface in the boundary layer that influence

the simulated sub-grid TI generated by the boundary layer parameterization. Our analysis demonstrates the utility of identifying scale-dependent uncertainties of TI modeling, which allows us to isolate the causes of errors in the simulated TI.

5.4.2 California coast

5.4.2.1 Simulated near-sea-surface wind, turbulence, and air-sea temperature gradient

We examined simulated near-surface wind and turbulence as well as corresponding air-sea gradient. Figure 20 highlights the results for the baseline simulation at Morro Bay in December 2020. The time series of air-sea temperature differences indicates there were several periods with convective conditions (SST is larger than air temperature; red patches in the time series of SST − T_{air}) simulated. Correspondingly, larger wind speed (mostly associated with northerly winds) and larger turbulence kinetic energy and TI appear in those periods. This implies that the advected air from the north could be a primary factor in modulating the near-surface stability during this winter month.

Figure 20. Wind speed (WSPD), wind direction (WDIR), sea-air temperature difference (SST − T_{air}), turbulence kinetic energy (TKE), and turbulence intensity (TI) as simulated by baseline simulation at Morro Bay from Dec. 1–28, 2020.

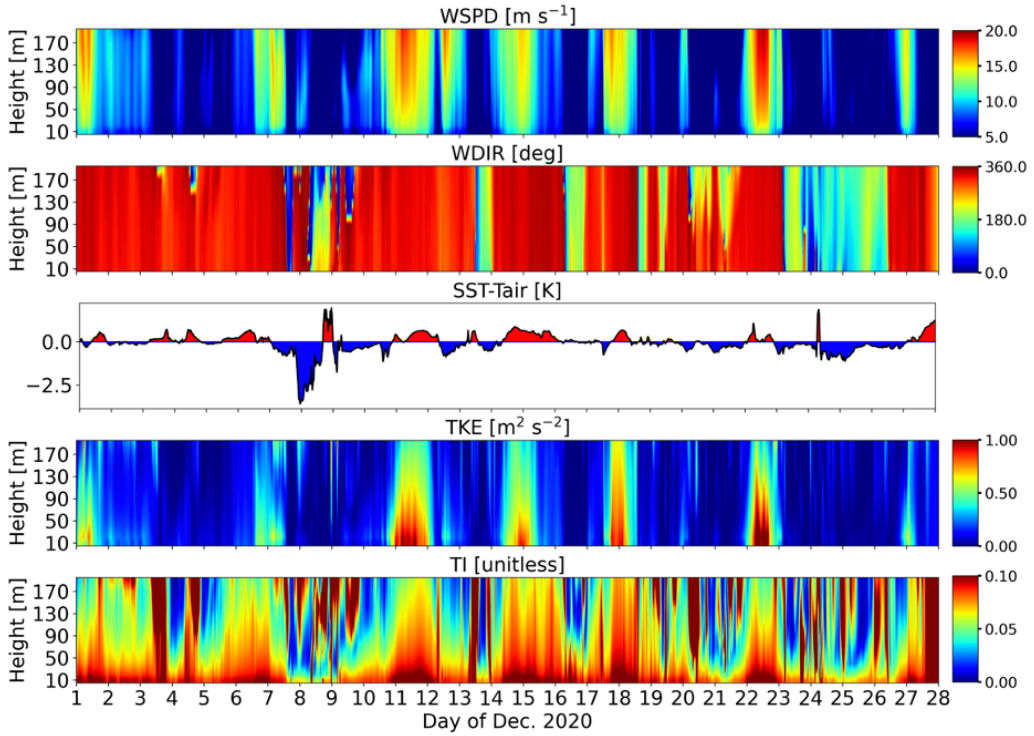

5.4.2.2 Monthly statistics

We calculated the monthly statistics of simulated sea-air temperature difference and hub-height (~80m) wind speed, TKE, and TI for each month. Figure 21 and Figure 22 display the results for Humboldt and Morro Bay, respectively. Overall, the monthly trend of wind speed is consistent between two offshore sites. For instance, wind speed is largest in May (2021), followed by June (2021), November (2020), and December (2020). Nevertheless, the differences between the two locations vary by month. For example, the mean wind speed difference in June can be as large as 2 m s^{-1}, whereas only slight differences are seen in other months.

The temperature contrast between the sea surface and air at 2-m is again used here as an indicator of near-surface stability. At Humboldt, the sea-air temperature difference transitioned from slightly positive (convective) to more negative (stable) from early winter to early summer. The least unstable conditions are found in May. Normally, one expects to see larger TKE in unstable conditions. However, we found that TKE is largest in May at both locations when sea-air temperature difference was modest. This implies that other processes, such as wind shear, contribute to the production of TKE. In addition, it is evident that simulated atmospheric conditions are more frequently unstable at Morro Bay than at Humboldt. Correspondingly, the TKE values are larger at Morro Bay than at Humboldt. Since TI is a function of wind speed and TKE, TI is larger when there is relatively large TKE and small wind speed. It is logical that TI is generally larger in Morro Bay than in Humboldt, as the relative difference in wind speed between the two sites is much smaller compared to the TKE difference.

The impact of the SST data on these properties can also be derived from the comparisons between the baseline and *sstupdate* simulations. Monthly trends may be directly impacted by the sea-air temperature difference. The temperature differences shift toward positive values, which means more unstable conditions are represented in the model with the application of finer-resolution SST. While TKE slightly increases with the change in SST forcing, wind speed has the least response to it. As a result, TI becomes correspondingly larger.

Figure 21. Simulated monthly mean and standard deviation of sea-air temperature difference, hub-height wind speed, TKE, and TI. The mean and standard deviation are represented by colored bars and gray error bars, respectively. Results obtained at Humboldt site for November 2020, December 2020, May 2021, and June 2021 are displayed.

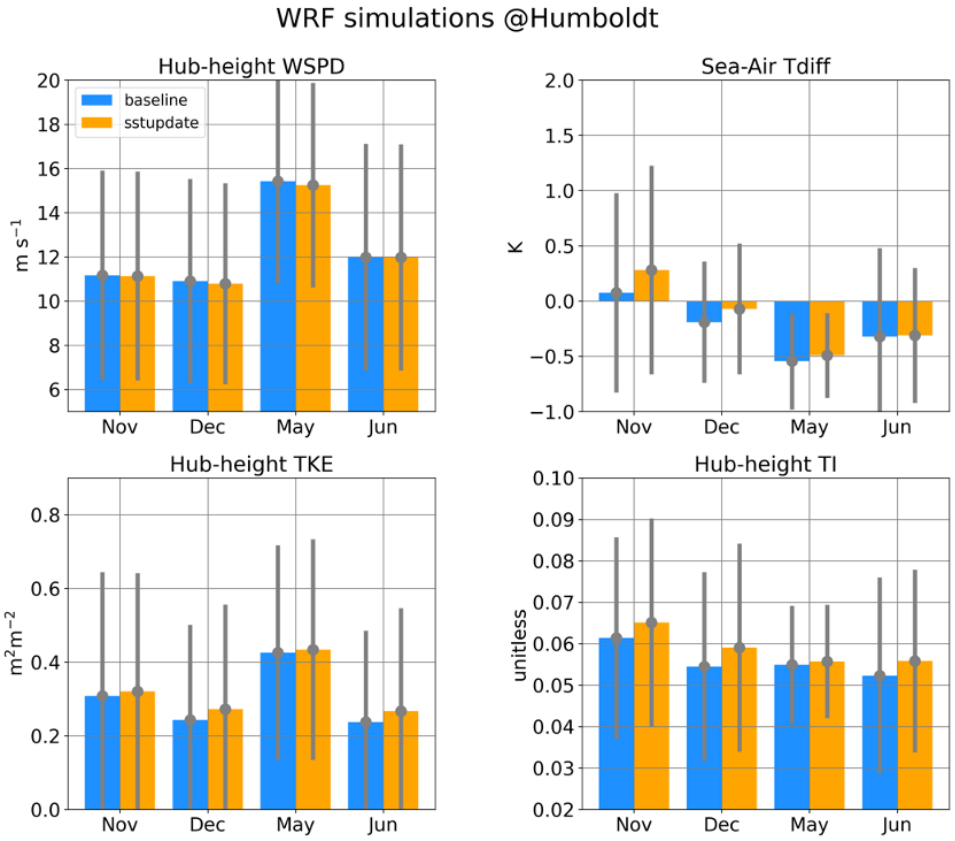

Figure 22. Same as Figure 12, but for Morro Bay.

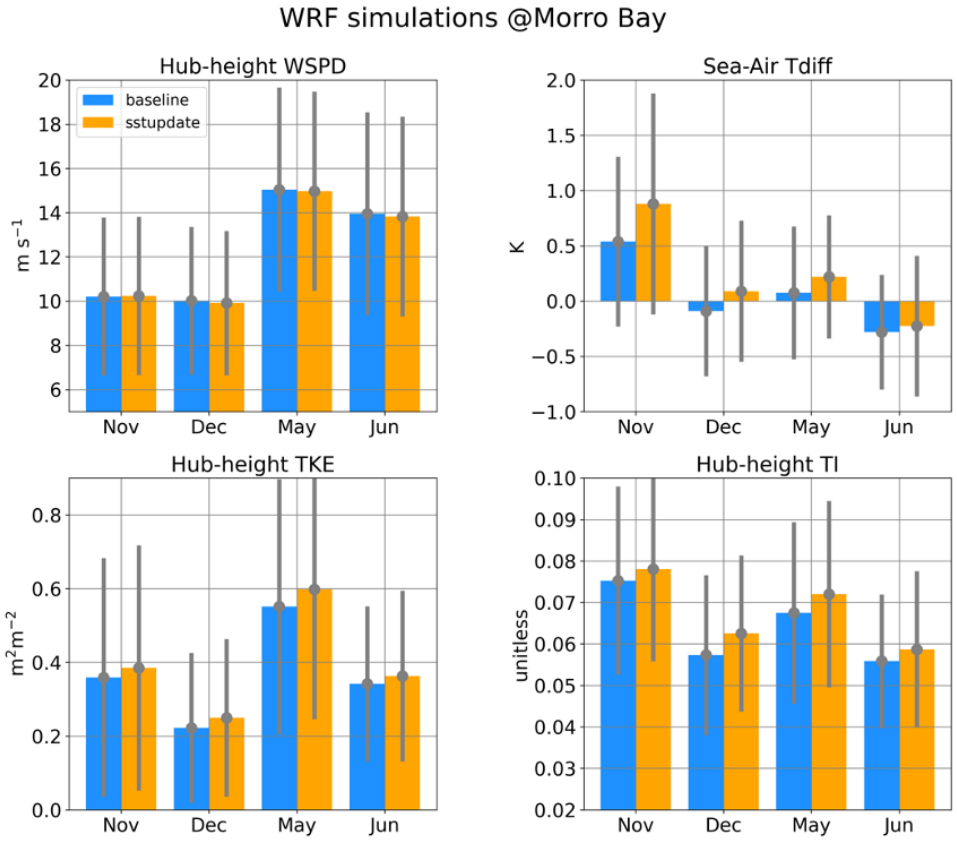

5.4.2.3 Evaluation of simulated hub-height wind and near-sea-surface properties

Observations collected by instruments deployed on the lidar buoys are used to evaluate our simulations. Comparisons of variables such as SST, 2-m temperature and relative humidity, and 80-m wind speed and wind direction are given in Figure 23 and Figure 24. Note that the lidar buoy at Humboldt was not in full operation until May 24, 2021; thus, the results from that location are not shown.

The model validation for the Humboldt site (Figure 23) indicates that the high-resolution SST data provide a more realistic representation of SST, even though the time series was still smoother than what was measured by the buoy. The updated SST forcing significantly reduces cold biases in the SST forcing of the baseline simulation. While there are short periods with relatively larger biases across different variables, the result shows that the simulations capture most of the mesoscale weather events that likely drive the day-to-day variations.

Results for the Morro Bay site are shown in Figure 24. We note that the 2-m relative humidity observation is not valid for June in 2021. The comparisons in SST time series indicate that warm biases exist in the Jet Propulsion Laboratory SST product at this location, except for November of 2020. The warm bias in the model lower boundary leads to warmer and drier atmospheric conditions at 2 m, which essentially lower the model skill in predicting thermodynamic fields near the sea surface. The impact of the SST forcing on the wind fields at 80 m is smaller than on near-surface temperature and humidity, as the differences between the 80-m winds from two simulations are subtle.

Figure 23. Time series comparisons of sea surface temperature (SST), 2-m temperature and relative humidity, 80-m wind speed and wind direction at Humboldt in November and December 2020, and June 2021. Lines or markers in red, blue, and black represent results from the *sstupdate* simulation, baseline simulation, and lidar observations, respectively.

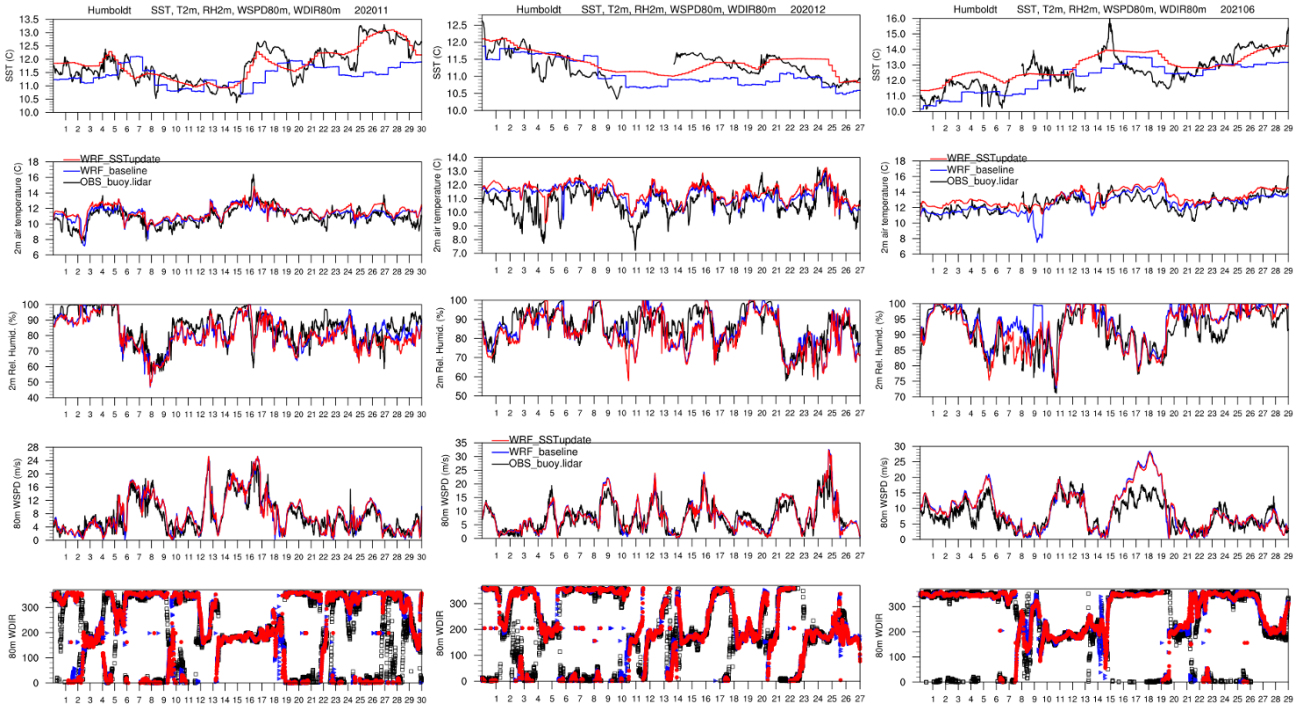

Figure 24. Same as Figure 23 but for the location at Morro Bay.

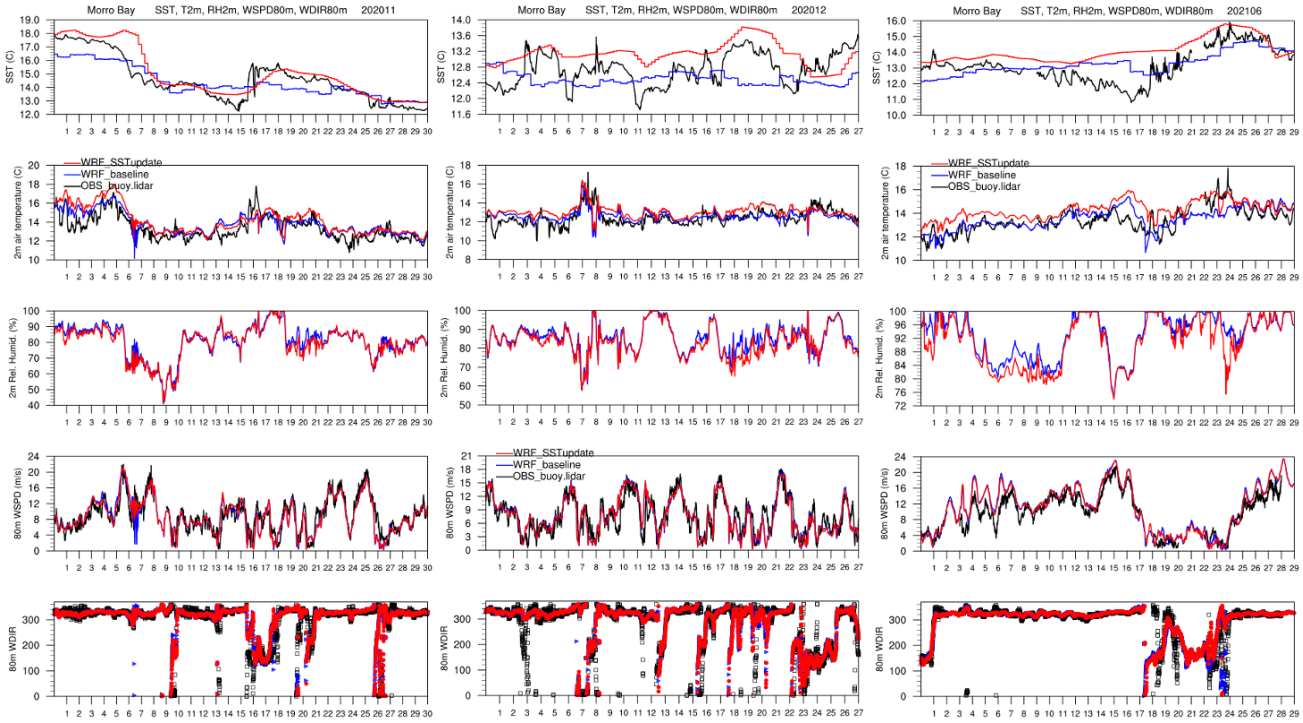

5.4.2.4 Comparison of turbulence intensity

Compared to a fixed lidar, a buoy-mounted lidar bobs with the waves, which makes an accurate calculation of turbulence information from floating lidars extremely challenging. It is thus necessary to assess the turbulence data measured with the lidar buoy before using it to evaluate turbulence properties. After examination of the 1-Hz WindCube data, we found that the notably large TKE and TI are most likely due to high noise levels in the wind profiles. The noise can be attributed to a failure of the WindCube's inertial measurement unit (IMU). Fortunately, there is an external IMU that has better data quality than the one equipped with the WindCube.

As documented in Krishnamurthy et al. (2023), to reprocess the data set, we first perform retrieval of the wind profile using the Leosphere (hybrid) algorithm, which produces wind profiles in the lidar frame of reference. Then, the wind vectors at each level of the profile are rotated into the Earth frame of reference using the simultaneous roll, pitch, and yaw data from the backup IMU. The motion-corrected data recorded by the external IMU are thus used to compute a 10-min wind speed average and standard deviation. At the time of writing this report, the reprocessed data were available from mid-May 2021 to June 2022 at the Humboldt site and from October 2020 to October 2021 at the Morro Bay site.

Figure 25 shows the reprocessed lidar data of hub-height wind speed and turbulence intensity collected at Humboldt in June 2021 compared against corresponding model data. While the wind speed is only slightly changed after the reprocessing, the reduction in TI is significant, leading to a much better agreement in TI between the observations and simulations compared to the earlier versions of the data. Despite the reprocessing, the TI values are still generally larger than the simulated TI (with medians of 0.1064 for the lidar and ~0.05 for the simulations). Also, the large TI events (June 8–11, 14–16, and 20–23) are all well represented in simulations. We found that the relatively large difference in wind speed over the period of June 16–20 is sensitive to the choice of planetary boundary layer parameterization, as the wind speed bias is significantly reduced when switching the scheme from the MYNN scheme (current choice) to the YSU scheme. Liu et al. (in review) examined more cases and concluded that during ambient northerly flow conditions, a coastal warm bias appears in the MYNN simulations and leads to a modeled wind speed bias by altering the boundary layer thermodynamics.

Results for the same period (June 2021) at the Morro Bay site are shown in Figure 26. Similar to the results for Humboldt, we find that the range of reprocessed lidar data is now more reasonable than the previous version. With minimal changes in wind speed, the curve of reprocessed TI shifts toward much smaller values and is closer to the simulated curves. While the median of the data of the previous version is ~0.31, the median of the reprocessed lidar data is around 0.08, which again approaches the median of the two simulated curves (~0.057). These comparisons reveal that the reprocessed lidar hub-height TI data are of relatively good quality, including periods with both relatively large and small values of TI, and are available for a more comprehensive model assessment.

Figure 25. (a) Time series of hub-height wind speed and turbulence intensity from lidar observations at the Humboldt site in June 2021, including the raw and reprocessed (QC) data. Corresponding model data from baseline and *sstupdate* simulations are also displayed. Comparison of power density functions in both wind speed and turbulence intensity are given in (b) and (c).

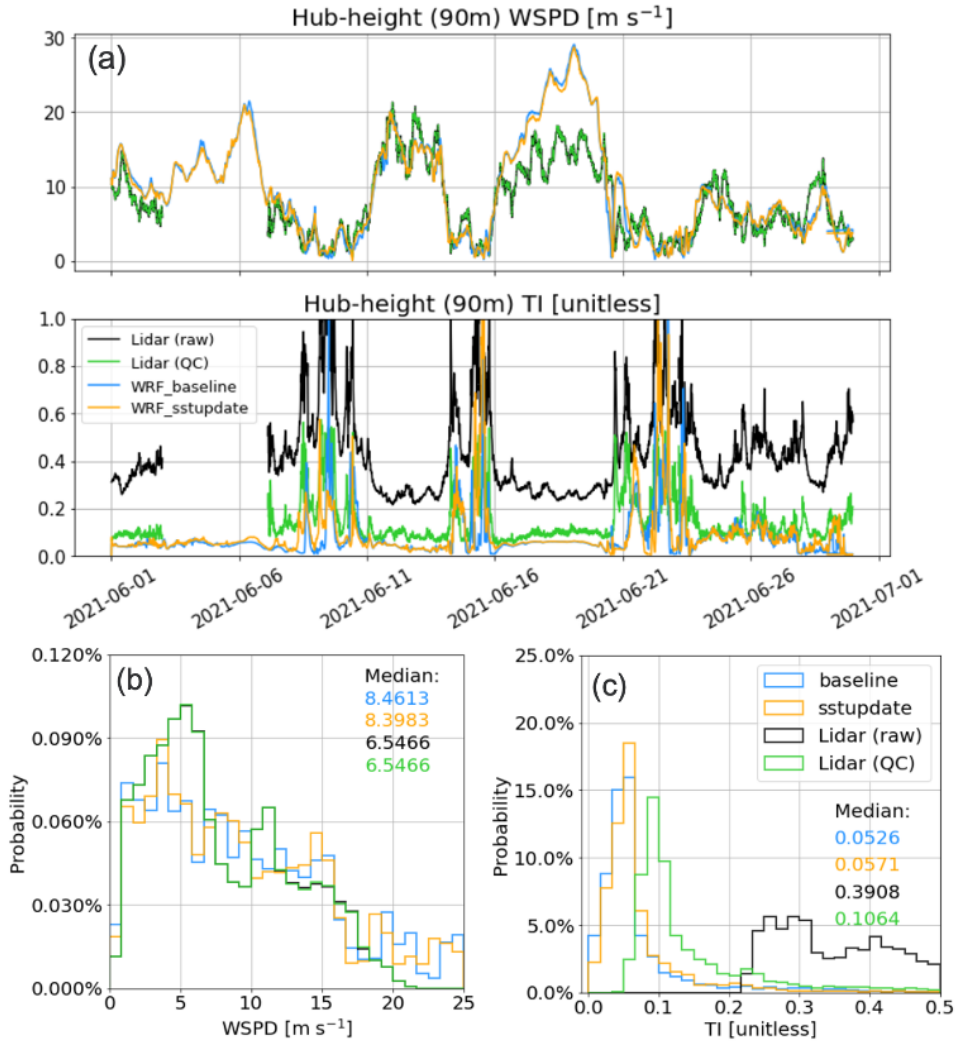

Figure 26. Same as Figure 25, but for the Morro Bay site in June 2020.

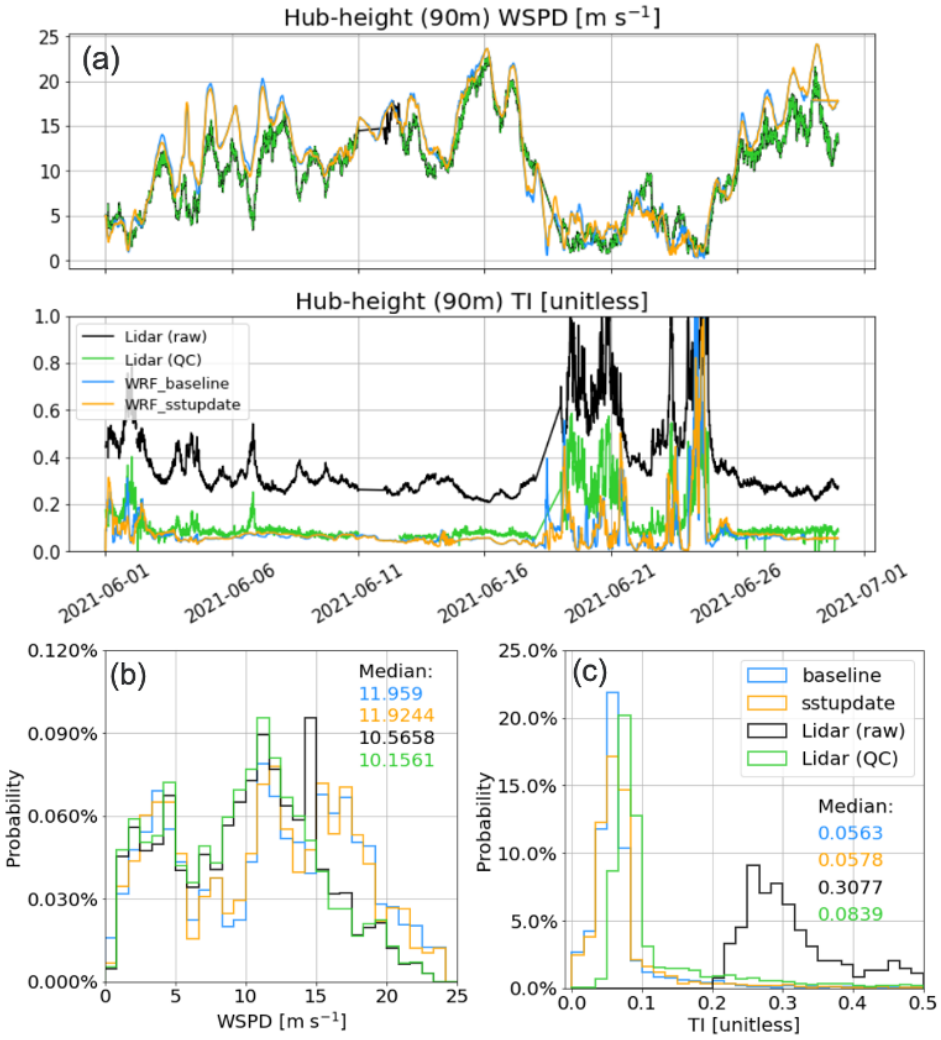

5.4.3 Gulf of Mexico

5.4.3.1 Statistical comparison of lidar measurements

We examined the data measured by both lidar wind profilers as deployed on the Ursa and Mars TLPs for the purpose of cross-validation. The probability density functions of TI and wind direction for each site are given in Figure 27. We note that the lidar data samples from the two lidars are not entirely overlapped in time. At the Ursa site, the most frequently observed values for TI and wind direction at hub height are approximately 0.08 and 150 degrees (~southeast), respectively. Similar distributions are seen in the results obtained from the lidar on TLP Mars. Given that the two TLPs are located relatively close to each other, it is not surprising that the two data sets generally have a good agreement. Nevertheless, distinct contrasts appear in the data measured at lowest heights (64 m and 70 m). For instance, in the PDFs of the TLP Ursa lidar at 64-m height, there are wider tails for TI (larger than 0.2) and wind direction (from 150

to 180 degrees, southeast to south). For wind speed, a large fraction of data resides in the bins below 3 m s^{-1} (not shown). In the results from TLP Mars, the differences between the lowest level (70 m) and levels above are much smaller. This is most likely due to contamination of lidar wind measurements, as the lower-elevation scans are likely influenced by cranes and other superstructure on the TLP Ursa.

Figure 27. Probability density functions of TI, wind speed (WSPD), and wind direction (WDIR) as observed by a lidar wind profiler mounted on TLP Ursa (a and b) and TLP Mars (c and d). The lidar data are sampled from March 2017 to October 2022 at TLP Ursa and from November 2017 to January 2023 at TLP Mars. The colors in the legend indicate the heights of measurements in meters. The color-coded median values are given in each panel.

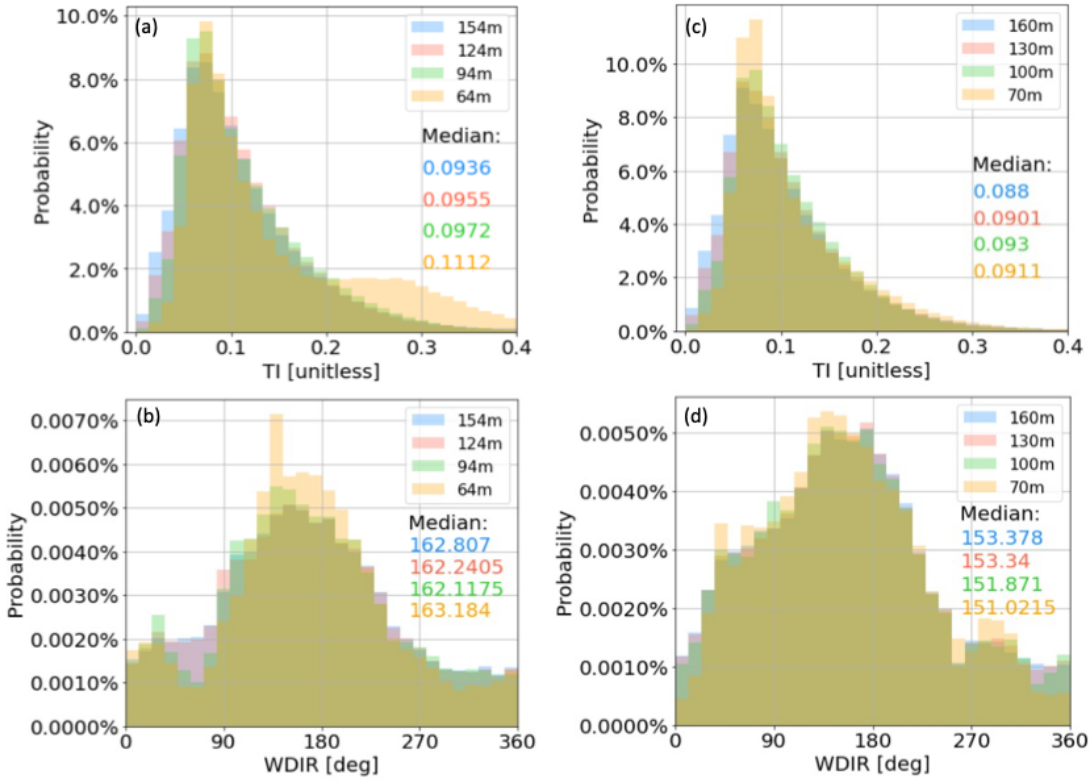

We also break down the two TI data sets by year and illustrate them with box and whisker plots (Figure 28). While there is interannual variability from 2017 to 2022 (data from both lidars show similar trends), the median value (~0.09) and annual variability (indicated by the boxes) are relatively consistent throughout the 6 years. Since the amount of missing data varies from one year to another, the spectrum of the PDF could shift accordingly, depending on which period of the year is missing.

Figure 28. Box and whisker plots of lidar-observed TI from 2017 to 2022 for TLP Ursa (top) and TLP Mars (bottom). The box for each year represents the middle 50% of scores (25% (Q1) to 75% (Q3)) for the data set. The difference between Q1 and Q3 is the inter-quartile range (IQR). The black line in the box denotes the median (Q3). The upper and lower ends of whiskers indicate Q1-1.5*IQR and Q3+1.5*IQR, respectively.

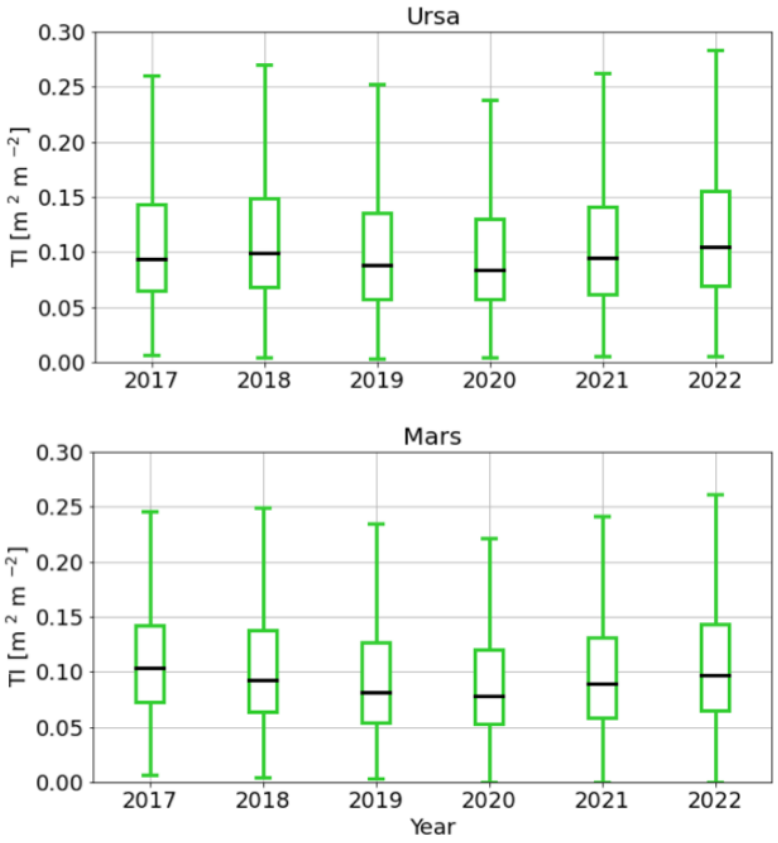

5.4.3.2 Model-observation comparison

Simulations are carried out with only the *sstupdate* configuration for the period from January to June of 2020. We examined the differences between the simulated and observed TI and wind speed. The results for January 2020 are highlighted here (Figure 29). Overall, the model tends to simulate larger TI values than those observed (median: ~0.02) and smaller wind speeds (median: ~ −0.5 m s^{-1}), except for the lowest level at each location (64 m and 70 m). This result is not consistent with the results obtained in the other two offshore regions (Mid-Atlantic and California coast). In those two cases, the model in general underestimates TI and simulates larger wind speeds. At the lowest levels, the reduced TI differences are most likely caused by the contaminated data, which have much larger TI and smaller wind speeds. While a model bias in wind speed can lead to TI errors, the uncertainty in simulated TKE may also contribute to the overall positive bias in TI. An assessment of simulated TKE is necessary for the next steps to isolate the contributions from the two components.

Figure 29. Probability density functions of TI and wind speed differences (model − observation) as computed for TLP Ursa (a and b) and TLP Mars (c and d) in January 2020. The colors in the legend denote the heights of measurements. The color-coded median values are given in each panel.

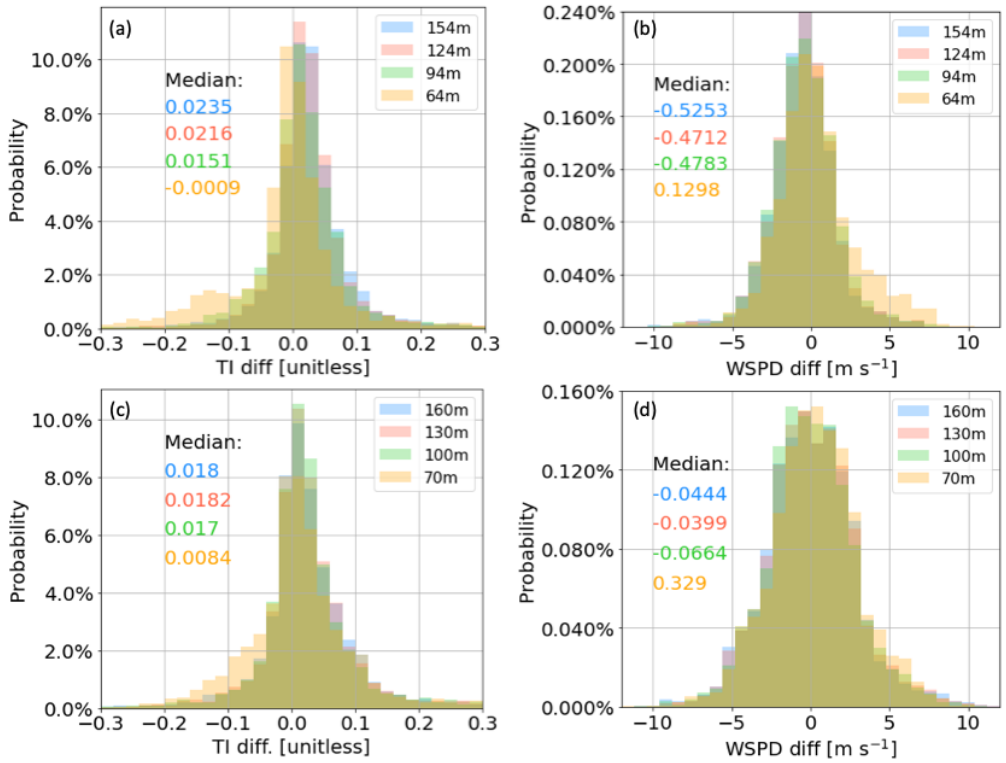

5.5 Summary

The algorithms for turbulence intensity derivations have been successfully implemented in the standard version of the WRF model. Simulated TI is divided into two components depending on the scale, including sub-grid and grid-resolved TI. While the sub-grid TI is diagnosed from parameterized turbulence kinetic energy through the MYNN PBL parameterization, the grid-resolved TI is estimated by using the model-resolved wind variances. The performance of the modeled TI is assessed in three different offshore regions—Mid-Atlantic, California coast, and Gulf of Mexico—by using multi-month observational data as collected at corresponding sites in each region. The analyzed results are summarized as follows:

- At offshore sites in the Mid-Atlantic and California coast, the simulated TI is smaller overall than the observed TI, regardless of altitude. On the other hand, in the two Gulf of Mexico sites, the model tends to produce larger TI than what was observed. While wind speed errors may partially contribute to the TI biases, the model uncertainty in representing TKE is also key to further improve TI simulation.
- The MYNN PBL scheme reacts reasonably to changes in the vertical temperature gradient from one location to another and from time to time. The validation carried out for the MVCO ASIT

(in the Mid-Atlantic) indicates that simulated TKE is generally smaller than what is observed by the lidar, especially for events with large TKE values. Future work can focus on using TKE observations collected in other regions to complete a cross-validation.

- While wind speed bias is generally smaller in simulations for the Mid-Atlantic and California coast, relatively large negative wind speed biases are seen for sites in the Gulf of Mexico. This is likely the reason why TI is significantly overpredicted in this region.
- Directly summing up sub-grid and resolved TI may not improve the TI prediction, because the uncertainty induced by unrealistic representation of mesoscale weather systems, including timing errors, will be also introduced in this manner.
- The WRF model generally struggles in predicting weak TI due to weaker forcings associated with smaller sea-air temperature differences and likely small surface heat fluxes.
- Overall, cold bias in the SST of the baseline simulation is effectively reduced by substituting it with more accurate SST forcing. This reduces model biases in near-surface air temperature as well as hub-height wind speed and TI for the site in the Mid-Atlantic.
- Data reprocessing for buoy lidar measurements is a necessary step and is shown to substantially improve the data quality.
- The lidar data analysis for the sites in the Gulf of Mexico indicates that the lowest level of lidar data is contaminated, which is most likely caused by beam blockage by the cranes operated on the oil platform. Measurements at high altitudes, however, appear to be free of this issue.

6 Conclusions

The NOW-23 data set is a comprehensive offshore-focused wind resource assessment data set that is freely available and expected to play a crucial role in supporting the growth of the offshore wind energy sector in the United States. This report has outlined the regionally focused approach utilized to generate the data set for each U.S. offshore region. The NOW-23 data set is anticipated to supersede NREL's WIND Toolkit for all offshore analyses and become one of the most widely utilized data sets for offshore wind resource assessments in the United States. The findings obtained from the analysis underscore the significance of conducting regionally focused validation and careful model setup selection while leveraging as many available observational data sets as possible. This analysis showcases the interdependent relationship between NWP models and observations, emphasizing their mutual benefits. To mitigate the inherent uncertainties in numerical models, it is essential to increase the availability of long-term observational data. Sharing proprietary observational data sets can be a viable approach to achieve this goal. When evaluating the costs and benefits associated with data-sharing initiatives, it is important for stakeholders to recognize the long-term advantages stemming from enhanced numerical modeling capabilities facilitated by access to additional observational data sets.

Further analysis and validation are required for the NOW-23 data set in Hawaii and the North Pacific regions, subject to future work pending funding availability. As more offshore observations become accessible, the existing validation efforts can be expanded to further validate the NOW-23 model setup in locations of interest for current and future offshore wind energy lease areas. Lastly, considering the unsatisfactory performance of the MYNN PBL scheme on the U.S. West Coast, additional analysis is warranted to delve into the causes of its failure in the region. Furthermore, it is crucial to propose and implement offshore-focused improvements to the parameterization scheme in order to enhance its performance.

7 References

Arthur, R. S., T. W. Juliano, B. Adler, R. Krishnamurthy, J. K. Lundquist, B. Kosović, and P. A. Jiménez, 2022: Improved Representation of Horizontal Variability and Turbulence in Mesoscale Simulations of an Extended Cold-Air Pool Event. *Journal of Applied Meteorology and Climatology*, 61, 685–707, https://doi.org/10.1175/JAMC-D-21-0138.1.

Bardal, L. M., and L. R. Sætran, 2017: Influence of Turbulence Intensity on Wind Turbine Power Curves. *Energy Procedia*, 137, 553–558, https://doi.org/10.1016/j.egypro.2017.10.384.

Bardal, L. M., A. E. Onstad, L. R. Sætran, and J. A. Lund, 2018: Evaluation of Methods for Estimating Atmospheric Stability at Two Coastal Sites. *Wind Engineering*, 42, 561–575, https://doi.org/10.1177/0309524X18780378.

Benjamin, S. G., S. S. Weygandt, J. M. Brown, M. Hu, C. R. Alexander, T. G. Smirnova, J. B. Olson, et al., 2016: A North American Hourly Assimilation and Model Forecast Cycle: The Rapid Refresh. *Monthly Weather Review*, 144, 1669–1694, https://doi.org/10.1175/MWR-D-15-0242.1.

Bodini, N., J. K. Lundquist, and A. Kirincich, 2020: Offshore Wind Turbines Will Encounter Very Low Atmospheric Turbulence. *J. Phys.: Conf. Ser*., 1452, 012023, https://doi.org/10.1088/1742-6596/1452/1/012023.

Bodini, N., W. Hu, M. Optis, G. Cervone, and S. Alessandrini, 2021: Assessing Boundary Condition and Parametric Uncertainty in Numerical-Weather-Prediction-Modeled, Long-Term Offshore Wind Speed Through Machine Learning and Analog Ensemble, *Wind Energy Science,* 6, 1363–1377, https://doi.org/10.5194/wes-6-1363-2021.

Bodini, N., A. Rybchuk, M. Optis, W. Musial, J. K. Lundquist, S. Redfern, C. Draxl, R. Krishnamurthy, and B. Gaudet. 2022: Update on NREL's 2020 Offshore Wind Resource Assessment for the California Pacific Outer Continental Shelf. Golden, CO: National Renewable Energy Laboratory. NREL/TP-5000-83756.

Bodini, N., S. Castagneri, and M. Optis, 2023: Long-Term Uncertainty Quantification in WRF-Modeled Offshore Wind Resource Off the US Atlantic Coast, *Wind Energy Science,* 8, 607–620, https://doi.org/10.5194/wes-8-607-2023.

Bodini, N., M. Optis, S. Redfern, D. Rosencrans, A. Rybchuk, J. K. Lundquist, V. Pronk, S. Castagneri, A. Purkayastha, C. Draxl, R. Krishnamurthy, E. Young, B. Roberts, E. Rosenlieb, and W. Musial, in review: The 2023 National Offshore Wind Data Set (NOW-23), *Earth System Science Data Discussions* [preprint], https://doi.org/10.5194/essd-2023-490, in review, 2023.

Chen, F., and J. Dudhia, 2001: Coupling an Advanced Land Surface–Hydrology Model with the Penn State–NCAR MM5 Modeling System. Part I: Model Implementation and Sensitivity. *Monthly Weather Review*, 129, 569–585, https://doi.org/10.1175/1520-0493(2001)129<0569:CAALSH>2.0.CO;2.

Chin, T. M., J. Vazquez-Cuervo, and E. M. Armstrong, 2017: A Multi-Scale High-Resolution Analysis of Global Sea Surface Temperature. *Remote Sensing of Environment*, 200, 154–169, https://doi.org/10.1016/j.rse.2017.07.029.

Clifton, A., and J. K. Lundquist, 2012: Data Clustering Reveals Climate Impacts on Local Wind Phenomena. *Journal of Applied Meteorology and Climatology* 51, no. 8 (2012): 1547–1557, https://doi.org/10.1175/JAMC-D-11-0227.1.

Clifton, A., and R. Wagner, 2014: Accounting for the Effect of Turbulence on Wind Turbine Power Curves. *J. Phys.: Conf. Ser*., 524, 012109, https://doi.org/10.1088/1742-6596/524/1/012109.

Donlon, C. J., M. Martin, J. Stark, J. Roberts-Jones, E. Fiedler, and W. Wimmer, 2012: The Operational Sea Surface Temperature and Sea Ice Analysis (OSTIA) system. *Remote Sensing of Environment*, 116, 140–158, https://doi.org/10.1016/j.rse.2010.10.017.

Draxl, C., A. Clifton, B. M. Hodge, and J. McCaa, 2015a: The Wind Integration National Dataset (WIND) Toolkit. *Applied Energy*, 151, 355–366, https://doi.org/10.1016/j.apenergy.2015.03.121.

Draxl, C., B. M. Hodge, A. Clifton, and J. McCaa, 2015b: Overview and Meteorological Validation of the Wind Integration National Dataset Toolkit. Golden, CO: National Renewable Energy Laboratory. NREL/TP-5000-61740.

Fernando, H. J. S., J. Mann, J. M. L. M. Palma, J. K. Lundquist, R. J. Barthelmie, M. Belo-Pereira, ... and Y. Wang, 2019: The Perdigão: Peering into Microscale Details of Mountain Winds. *Bulletin of the American Meteorological Society*, 100(5), 799–819, https://doi.org/10.1175/BAMS-D-17-0227.1.

Fitch, A. C., J. B. Olson, J. K. Lundquist, J. Dudhia, A. K. Gupta, J. Michalakes, and I. Barstad, 2012: Local and Mesoscale Impacts of Wind Farms as Parameterized in a Mesoscale NWP Model, *Monthly Weather Review,* 140, 3017–3038, https://doi.org/10.1175/MWR-D-11-00352.1.

Gelaro, R., W. McCarty, M. J. Suárez, R. Todling, A. Molod, L. Takacs, ... and B. Zhao, 2017: The Modern-Era Retrospective Analysis for Research and Applications, Version 2 (MERRA-2). *Journal of Climate*, 30(14), 5419–5454, https://doi.org/10.1175/JCLI-D-16-0758.1.

Grell, G. A., J. Dudhia, and D. R. Stauffer, 1994: A Description of the Fifth-Generation Penn State/NCAR Mesoscale Model (MM5). University Corporation for Atmospheric Research. NCAR/TN-398+STR. doi:10.5065/D60Z716B.

Hahmann, A. N., T. Sīle, B. Witha, N. N. Davis, M. Dörenkämper, Y. Ezber, ... and S. Söderberg, 2020: The Making of the New European Wind Atlas–Part 1: Model Sensitivity. *Geoscientific Model Development*, 13(10), 5053–5078, https://doi.org/10.5194/gmd-13-5053-2020.

Hansen, K. S., R. J. Barthelmie, L. E. Jensen, and A. Sommer, 2012: The impact of turbulence intensity and atmospheric stability on power deficits due to wind turbine wakes at Horns Rev wind farm. *Wind Energy*, 15, 183–196, https://doi.org/10.1002/we.512.

Hersbach, H., Bell, B., Berrisford, P., Hirahara, S., Horányi, A., Muñoz-Sabater, J., ... and Thépaut, J. N., 2020: The ERA5 Global Reanalysis. *Quarterly Journal of the Royal Meteorological Society*, 146(730), 1999–2049, https://doi.org/10.1002/qj.3803.

Hirahara, S., Balmaseda, M. A., Boisseson, E. D., and Hersbach, H., 2016: 26 Sea Surface Temperature and Sea Ice Concentration for ERA5. Eur. Centre Medium Range Weather Forecasts, Berkshire, UK, ERA Rep. Ser, 26.

Hong, S.-Y., Y. Noh, and J. Dudhia, 2006: A New Vertical Diffusion Package with an Explicit Treatment of Entrainment Processes. *Monthly Weather Review*, 134, 2318–2341, https://doi.org/10.1175/MWR3199.1.

Howland, M. F., C. M. González, J. J. P. Martínez, J. B. Quesada, F. P. Larrañaga, N. K. Yadav, J. S. Chawla, and J. O. Dabiri, 2020: Influence of Atmospheric Conditions on the Power Production of Utility-Scale Wind Turbines in Yaw Misalignment. *Journal of Renewable and Sustainable Energy*, 12, 063307, https://doi.org/10.1063/5.0023746.

Hsu, S. A., 1989: The Relationship Between the Monin-Obukhov Stability Parameter and the Bulk Richardson Number at Sea. *Journal of Geophysical Research: Oceans*, 94, 8053–8054, https://doi.org/10.1029/JC094iC06p08053.

Iacono, M. J., J. S. Delamere, E. J. Mlawer, M. W. Shephard, S. A. Clough, and W. D. Collins, 2008: Radiative Forcing by Long-Lived Greenhouse Gases: Calculations with the AER Radiative Transfer Models. *Journal of Geophysical Research: Atmospheres*, 113, https://doi.org/10.1029/2008JD009944.

Jiménez, P. A., Dudhia, J., González-Rouco, J. F., Navarro, J., Montávez, J. P., and García-Bustamante, E., 2012: A Revised Scheme for the WRF Surface Layer Formulation. *Monthly Weather Review*, 140(3), 898–918, https://doi.org/10.1175/MWR-D-11-00056.1.

Juliano, T. W., Kosović, B., Jiménez, P. A., Eghdami, M., Haupt, S. E., and Martilli, A., 2022: "Gray Zone" Simulations Using a Three-Dimensional Planetary Boundary Layer Parameterization in the Weather Research and Forecasting Model, *Monthly Weather Review*, 150, 1585–1619, https://doi.org/10.1175/MWR-D-21-0164.1.

Kaiser, K., W. Langreder, H. Hohlen, and J. Højstrup, 2007: Turbulence Correction for Power Curves. Wind Energy, J. Peinke, P. Schaumann, and S. Barth, Eds., Berlin, Heidelberg, Springer, 159–162.

Kosović, B., Munoz, P. J., Juliano, T. W., Martilli, A., Eghdami, M., Barros, A. P., and Haupt, S. E., 2020: Three-Dimensional Planetary Boundary Layer Parameterization for High-Resolution Mesoscale Simulations, *J. Phys.: Conf. Ser.*, 1452, 012080, https://doi.org/10.1088/1742-6596/1452/1/012080.

Krishnamurthy, R., G. G. Medina, B. Gaudet, W. I. Gustafson Jr., E. I. Kassianov, J. Liu, R. K. Newsom, L. M. Sheridan, and A. M. Mahon, 2023: Year-long Buoy-Based Observations of the Air–Sea Transition Zone off the U.S. West Coast. *Earth System Science Data Discussions*, 1–53, https://doi.org/10.5194/essd-2023-115.

Liu, Y., R. Krishnamurthy, B. Gaudet, S.-L. Tai, L. K. Berg, N. Bodini, A. Rybchuk, and A. Kumler, under review: Identifying Meteorological Drivers for Errors in Modeled Winds Along the Northern California Coast. *Monthly Weather Review*

Nakanishi, M. and H. Niino, 2009: Development of an Improved Turbulence Closure Model for the Atmospheric Boundary Layer, *Journal of the Meteorological Society of Japan*. Ser. II, 87, 895–912, https://doi.org/10.2151/jmsj.87.895.

National Weather Service, 2014: Description of NCEP High Res. SST Analysis. NOAA. https://polar.ncep.noaa.gov/sst/ophi/description.shtml (Accessed March 15, 2023).

Niu, G.-Y., Z.-L. Yang, K. E. Mitchell, F. Chen, M. B. Ek, M. Barlage, … and Y. Xia: The Community Noah Land Surface Model with Multiparameterization Options (Noah-MP): 1. Model Description and Evaluation with Local-scale Measurements, *Journal of Geophysical Research: Atmospheres*, 116, 2011, https://doi.org/10.1029/2010JD015139.

Olson, J. B., T. Smirnova, J. S. Kenyon, D. D. Turner, J. M. Brown, W. Zheng, and B. W. Green, 2021: A Description of the MYNN Surface-layer Scheme. National Oceanic and Atmospheric Administration. OAR GSL-67. https://doi.org/10.25923/f6a8-bc75.

Optis, M., O. Rybchuk, N. Bodini, M. Rossol, and W. Musial., 2020a: 2020 Offshore Wind Resource Assessment for the California Pacific Outer Continental Shelf. Golden, CO: National Renewable Energy Laboratory. NREL/TP-5000-77642.

Optis, M., N. Bodini, M. Debnath, and P. Doubrawa, 2020b: Best Practices for the Validation of US Offshore Wind Resource Models. Golden, CO: National Renewable Energy Laboratory. NREL/TP-5000-78375.

Optis, M., A. Kumler, G. N. Scott, M. C. Debnath, and P. J. Moriarty, 2020c: Validation of RU-WRF, the Custom Atmospheric Mesoscale Model of the Rutgers Center for Ocean Observing Leadership. Golden, CO: National Renewable Energy Laboratory. NREL/TP-5000-75209.

Redfern, S., M. Optis, G. Xia, and C. Draxl, 2023: Offshore Wind Energy Forecasting Sensitivity to Sea Surface Temperature Input in the Mid-Atlantic, *Wind Energy Science*, 8, 1–23, https://doi.org/10.5194/wes-8-1-2023.

Rodrigo, J. S., E. Cantero, B. García, F. Borbón, U. Irigoyen, S. Lozano, P. M. Fernande, and R. A. Chávez, 2015: Atmospheric Stability Assessment for the Characterization of Offshore Wind Conditions. *J. Phys.: Conf. Ser.*, 625, 012044, https://doi.org/10.1088/1742-6596/625/1/012044.

Rosencrans, D., J. K. Lundquist, M. Optis, A. Rybchuk, N. Bodini, and M. Rossol, in review: Annual Variability of Wake Impacts on Mid-Atlantic Offshore Wind Plant Deployments, *Wind Energy Science Discussions* [preprint], https://doi.org/10.5194/wes-2023-38.

Rybchuk, A., T. W. Juliano, J. K. Lundquist, D. Rosencrans, N. Bodini, and M. Optis, 2022: The Sensitivity of the Fitch Wind Farm Parameterization to a Three-dimensional Planetary Boundary Layer Scheme, *Wind Energy Science*, 7, 2085–2098, https://doi.org/10.5194/wes-7-2085-2022.

Saint-Drenan, Y.-M., R. Besseau, M. Jansen, I. Staffell, A. Troccoli, L. Dubus, J. Schmidt, K. Gruber, S. G. Simões, and S. Heier, 2020: A Parametric Model for Wind Turbine Power Curves Incorporating Environmental Conditions. *Renewable Energy*, 157, 754–768, https://doi.org/10.1016/j.renene.2020.04.123.

Sathe, A., J. Mann, N. Vasiljevic, and G. Lea, 2015: A Six-beam Method to Measure Turbulence Statistics Using Ground-based Wind Lidars. *Atmospheric Measurement Techniques* 8, no. 2: 729–740, https://doi.org/10.5194/amt-8-729-2015.

Shaw, R. H., G. Den Hartog, K. M. King, and G. W. Thurtell, 1974: Measurements of Mean Wind Flow and Three-dimensional Turbulence Intensity Within a Mature Corn Canopy. *Agricultural Meteorology*, 13, 419–425, https://doi.org/10.1016/0002-1571(74)90082-X.

Shaw, W. J., L. K. Berg, J. Cline, C. Draxl, I. Djalalova, E. P. Grimit, ... and J. M. Wilczak, 2019: The Second Wind Forecast Improvement Project (WFIP2): General Overview. *Bulletin of the American Meteorological Society*, 100(9), 1687–1699, https://doi.org/10.1175/BAMS-D-18-0036.1.

Skamarock, W. C., J. B. Klemp, J. Dudhia, D. O. Gill, Z. Liu, J. Berner, ... and X. Y. Huang, 2019: A Description of the Advanced Research WRF Model Version 4. National Center for Atmospheric Research: Boulder, CO, USA, 145(145), 550.

Sullivan, P. P., J. C. McWilliams, J. C. Weil, E. G. Patton, and H. J. S. Fernando, 2020: Marine Boundary Layers above Heterogeneous SST: Across-Front Winds. *Journal of the Atmospheric Sciences*, 77, 4251–4275, https://doi.org/10.1175/JAS-D-20-0062.1.

Tai, S.-L., L. K. Berg, R. Krishnamurthy, R. Newsom, and A. Kirincich, 2023: Validation of Turbulence Intensity as Simulated by the Weather Research and Forecasting Model off the US Northeast Coast, *Wind Energy Science*, 8, 433–448, https://doi.org/10.5194/wes-8-433-2023.

Taylor, K. E., 2001: Summarizing Multiple Aspects of Model Performance in a Single Diagram. *Journal of Geophysical Research: Atmospheres*. 106, no. D7: 7183–7192, https://doi.org/10.1029/2000JD900719.

Wharton, S., and J. K. Lundquist, 2012: Atmospheric Stability Affects Wind Turbine Power Collection. *Environmental Research Letters* 7, no. 1: 014005, https://doi.org/10.1088/1748-9326/7/1/014005.

Wilczak, J., C. Finley, J. Freedman, J. Cline, L. Bianco, J. Olson, ... and M. Marquis, 2015: The Wind Forecast Improvement Project (WFIP): A Public–Private Partnership Addressing Wind Energy Forecast Needs. *Bulletin of the American Meteorological Society*, 96(10), 1699–1718, https://doi.org/10.1175/BAMS-D-14-00107.1.

Zoumakis, N. M., and A. G. Kelessis, 1991: The Dependence of the Bulk Richardson Number on Stability in the Surface Layer. *Boundary-Layer Meteorology*, 57, 407–414, https://doi.org/10.1007/BF00120057.